



# Suppression of Composition $g$ -modes in Chemically Equilibrating Warm Neutron Stars

Tianqi Zhao<sup>1,2,3</sup> , Peter B. Rau<sup>2,4</sup> , Alexander Haber<sup>5,6</sup> , Steven P. Harris<sup>7</sup> , Constantinos Constantinou<sup>8,9</sup> , and Sophia Han<sup>10,11,12,3</sup>

<sup>1</sup> Department of Physics and Astronomy, Ohio University, Athens, OH 45701, USA

<sup>2</sup> Institute for Nuclear Theory, University of Washington, Seattle, WA 98195, USA

<sup>3</sup> Network for Neutrinos, Nuclear Astrophysics, and Symmetries (N3AS), University of California, Berkeley, CA 94720, USA

<sup>4</sup> Columbia Astrophysics Laboratory, Columbia University, New York, NY 10027, USA

<sup>5</sup> Mathematical Sciences and STAG Research Centre, University of Southampton, Southampton SO17 1BJ, UK

<sup>6</sup> Department of Physics, Washington University in St. Louis, St. Louis, MO 63130, USA

<sup>7</sup> Center for the Exploration of Energy and Matter and Department of Physics, Indiana University, Bloomington, IN 47405, USA

<sup>8</sup> INFN-TIFPA, Trento Institute of Fundamental Physics and Applications, Povo, 38123 TN, Italy

<sup>9</sup> European Centre for Theoretical Studies in Nuclear Physics and Related Areas, Villazzano, 38123 TN, Italy

<sup>10</sup> Tsung-Dao Lee Institute, Shanghai Jiao Tong University, Shanghai 201210, People's Republic of China; [sjhan@sjtu.edu.cn](mailto:sjhan@sjtu.edu.cn)

<sup>11</sup> School of Physics and Astronomy, Shanghai Jiao Tong University, Shanghai 200240, People's Republic of China

<sup>12</sup> State Key Laboratory of Dark Matter Physics, Shanghai Jiao Tong University, Shanghai 201210, People's Republic of China

Received 2025 May 8; revised 2025 August 28; accepted 2025 August 28; published 2025 October 31

## Abstract

We investigate the impact of chemical equilibration and the resulting bulk viscosity on nonradial oscillation modes of warm neutron stars at temperatures up to  $T \approx 5$  MeV, relevant for protoneutron stars and neutron star postmerger remnants. In this regime, the relaxation rate of weak interactions becomes comparable to the characteristic frequencies of composition  $g$ -modes in the core, resulting in resonant damping. To capture this effect, we introduce the dynamical sound speed, a complex, frequency-dependent generalization of the adiabatic sound speed that encodes both the restoring force and the dissipative effects of bulk compression. Using realistic weak reaction rates and three representative equations of state, we compute the complex frequencies of composition  $g$ -modes with finite-temperature profiles. We find that bulk viscous damping becomes increasingly significant with temperature and can completely suppress composition  $g$ -modes. In contrast, the  $f$ -mode remains largely unaffected by bulk viscosity due to its nearly divergence-free character. Our results highlight the sensitivity of  $g$ -mode behavior to thermal structure, weak reaction rates, and the equation of state, and establish the dynamical sound speed as a valuable descriptor characterizing oscillation properties in dissipative neutron star matter.

*Unified Astronomy Thesaurus concepts:* Neutron stars (1108); Nuclear astrophysics (1129)

## 1. Introduction

Asteroseismology is a key probe of stellar interiors, and when applied to neutron stars (NSs), can be used to provide information on their chemical composition and the dense matter equation of state (EOS; N. Andersson 2019; N. Andersson & B. Haskell 2024). Chemical composition is most sensitively probed by the  $g$ -modes, which are supported by gravity and a chemical composition gradient-driven buoyancy. These oscillation modes have frequencies in the tens to hundreds of Hz range. There is also an entropy gradient contribution to the buoyancy, but at typical temperatures for most of an NS's life ( $T \lesssim$  a few times  $10^8$  K), the chemical composition gradient is the dominant contribution to the  $g$ -mode, and purely thermal  $g$ -modes have frequencies of order a few Hz (P. N. McDermott et al. 1983) at these temperatures. The gradients of various particle species have been considered as the source of NS  $g$ -modes, starting with the proton fraction of total baryons (A. Reisenegger & P. Goldreich 1992). Later,  $g$ -modes due to the muon fraction of total leptons (usually in superfluid NSs) (E. M. Kantor & M. E. Gusakov 2014; V. A. Dommes & M. E. Gusakov 2016; A. Passamonti et al.

2016; H. Yu & N. N. Weinberg 2017; P. B. Rau & I. Wasserman 2018), hyperons (V. A. Dommes & M. E. Gusakov 2016; V. Tran et al. 2023), and quarks in the inner core (W. Wei et al. 2020; C. Constantinou et al. 2021; T. Zhao et al. 2022; D. Kumar et al. 2023) were studied.

Recently, large modifications to  $g$ -modes at  $T > 10$  MeV ( $\gtrsim 10^{11}$  K) have been shown due to the effect of finite temperature on the EOS (N. Lozano et al. 2022). At these temperatures, thermal contributions to  $g$ -modes are comparable to the composition gradient-driven buoyancy (V. Ferrari et al. 2003; F. Gittins & N. Andersson 2025). However, most calculations of NS  $g$ -modes that focused on the chemical-composition-driven modes have assumed cold (zero-temperature) NSs. This is a reasonable assumption for most of an NS's lifetime, since thermal effects on the mode spectrum for  $T \lesssim 100$  keV ( $\lesssim 10^9$  K) are generally very small and NSs cool below this within a few years after their birth (D. Page et al. 2004). The aforementioned references, including those that have included finite-temperature effects, thus typically assume infinitely slow chemical reaction rates, which is a good approximation for cold NSs as long as the weak reactions in standard nuclear matter responsible for restoring beta equilibrium in perturbed fluid elements are much slower than the oscillation frequency at these temperatures.

However, at temperatures in the MeV ( $\sim 10^{10}$  K) range, reaction rates are comparable to  $g$ -mode oscillation frequencies. These temperatures are unlikely to be reached in



Original content from this work may be used under the terms of the [Creative Commons Attribution 4.0 licence](https://creativecommons.org/licenses/by/4.0/). Any further distribution of this work must maintain attribution to the author(s) and the title of the work, journal citation and DOI.

inspiraling binary NSs (R. Counsell et al. 2024), where  $g$ -modes may be detectable (K. J. Kwon et al. 2024), since tidal excitation of oscillation modes are only expected to heat the stars to a few times  $10^8$  K prior to merger (D. Lai 1994; P. Arras & N. N. Weinberg 2019). MeV-range temperatures are thus relevant at two stages of an NS’s lifetime: (i) in young stars immediately after their birth in core-collapse supernovae, and (ii) in postmerger remnant NSs formed in binary mergers. For instance, the  $g$ -modes identified in numerical simulations as contributing to the gravitational-wave signal from protoneutron stars produced by core-collapse supernovae (V. Morozova et al. 2018; A. Torres-Forné et al. 2018; P. Jakobus et al. 2023; D. Vartanyan et al. 2023; N. E. Wolfe et al. 2023) will be modified by finite nuclear reaction rates, which was not considered in previous studies. These reactions give rise to bulk viscosity (S. P. Harris 2024), which has impacts across NS physics, including in damping radial oscillation modes (M. E. Gusakov et al. 2005),  $r$ -modes (N. Andersson et al. 1999), and as an energy dissipation mechanism in NS mergers (M. G. Alford et al. 2018). Bulk viscosity can be accounted for by including, in a reaction network, the underlying weak interaction rates (e.g., in radially oscillating NSs (M. E. Gusakov et al. 2005), in NSs at the edge of stability (E. Gourgoulhon & P. Haensel 1993; E. Gourgoulhon et al. 1995), for inspiraling NSs (P. Arras & N. N. Weinberg 2019) or in NS merger simulations (P. L. Espino et al. 2024; E. R. Most et al. 2024)), or through direct calculation of the bulk viscosity coefficient and implementation of dissipative relativistic hydrodynamics (e.g., in radially oscillating NSs (G. Camelió et al. 2023a, 2023b) or in NS merger simulations (M. Chabanov & L. Rezzolla 2025)).

The main modification to the dynamics of NS oscillations due to nuclear reactions is to damp the composition  $g$ -modes. In an early investigation, N. Andersson & P. Pnigouras (2019) performed a local plane-wave analysis of the Brunt–Väisälä frequency, showing how arbitrary nuclear reaction rates can introduce a complex component to the  $g$ -mode frequency, effectively damping the oscillations. Building on this, A. R. Counsell et al. (2024) extended the study by computing global  $g$ -modes in cold NSs using the BSk21 EOS. They showed that the real part of the  $g$ -mode frequency decreases while the imaginary part increases as the reaction rate is increased. Here, also, the  $g$ -mode properties were calculated as a function of the nuclear reaction rate—disconnected from its actual value in dense matter. In realistic NS matter, these rates depend sensitively on the local temperature and composition profiles, and should be computed self-consistently once a specific EOS is assumed.

To address this, we compute the  $g$ -modes of hot NSs, incorporating microphysically calculated temperature-dependent nuclear reaction rates consistent with the underlying EOS we use to compute the background stellar models and the oscillation modes. The physically grounded reaction rates lead to well-defined damping through bulk viscosity, moving beyond parametrized viscosity as in previous studies. By linking realistic microphysical inputs to global mode calculations, our approach enables a more accurate and self-consistent assessment of bulk viscous damping mechanisms in NSs under various thermal conditions. These rates have also been applied to examine the role of bulk viscosity in NS mergers through analyses of local density oscillations (M. G. Alford & S. P. Harris 2019; M. Alford et al. 2019; M. G. Alford

et al. 2024a), and numerical simulations (E. R. Most et al. 2024; M. Chabanov & L. Rezzolla 2025). To clarify, we only consider the chemical composition gradient  $g$ -modes at finite temperatures, and not the thermal  $g$ -mode contribution, since while we consider  $\sim$  MeV temperatures, we do not consider the  $T \gtrsim 10$  MeV temperatures at which the thermal contribution to  $g$ -modes is comparable to the chemical composition. Our quasinormal mode calculations use the zero-temperature EOS. Since the EOS and the susceptibilities required to calculate the dynamic speed of sound show a very weak temperature dependence in the temperature range studied here, we use the  $T=0$  approximation for those quantities, as justified in Appendix A. Only the calculation of the weak interaction rates and the calculation of the constant-entropy temperature profiles include (as they must) temperature. We also ignore the effects of nucleonic superfluidity-superconductivity, assuming that Cooper pairing between nucleons is destroyed at the temperatures of interest, which are generally well above the critical temperatures for the  $p$ -wave-paired neutron superfluidity ( $T_{cn} \sim 10^9$  K) and  $s$ -wave-paired proton superconductivity ( $T_{cp} \sim 7 \times 10^9$  K) expected to be found in NS cores (A. Sedrakian & J. W. Clark 2019).

In Section 2 we discuss the origin of bulk viscosity in NSs and introduce the concept of the dynamical sound speed, which directly encodes the effects of bulk viscosity. This formalism can be naturally incorporated into the eigenvalue problem for calculating  $g$ -mode frequencies in hot NSs, which we summarize in Section 3. We discuss the resulting changes to the  $g$ - and  $f$ -mode spectra of hot NSs due to bulk viscosity in Section 4, considering both isothermal and isentropic temperature profiles. Our conclusions and possible extensions of this work are presented in Section 5. We work in  $c = \hbar = 1$  units.

## 2. Bulk Viscosity and Dynamical Sound Speed

Finite temperature, neutrinoless  $npe$  matter out of chemical equilibrium is described by specifying the pressure  $p(n_B, \delta\mu, T)$ , where  $n_B$  is the baryon number density,  $T$  is the temperature, and the degree to which the matter is out of beta equilibrium (used interchangeably with “chemical equilibrium” in this work), is

$$\delta\mu \equiv \mu_n - \mu_p - \mu_e. \quad (1)$$

At sufficiently high temperatures, the neutrino mean free path shrinks (L. F. Roberts & S. Reddy 2017; M. G. Alford & S. P. Harris 2018) and neutrinos become trapped, and the definition of beta equilibrium is modified (M. Alford et al. 2019; A. R. Raduta et al. 2020). Neutrino-trapping effects are likely present at the higher end of the temperature range we consider here, but we neglect neutrino trapping for simplicity. The effect of neutrino-trapping on compositional  $g$ -mode frequencies has not been studied. Instead of specifying the temperature, it is sometimes convenient to instead specify the entropy per baryon  $S \equiv s/n_B$ , so that the pressure becomes the function  $p(n_B, \delta\mu, S)$ . A local, adiabatic, perturbation to the pressure  $p(n_B, \delta\mu, S)$  is given by

$$\Delta p = \left. \frac{\partial p}{\partial n_B} \right|_{\delta\mu, S} \Delta n_B + \left. \frac{\partial p}{\partial \delta\mu} \right|_{n_B, S} \Delta \delta\mu. \quad (2)$$

The proton fraction,  $x \equiv n_p/n_B$ , in beta equilibrium becomes a function of density and temperature  $x_{eq}(n_B, T)$ . This can be

calculated for various EOSs. When the proton fraction is away from its beta equilibrium value by an amount  $\delta x = x - x_{\text{eq}}$ , the system is out of chemical equilibrium by an amount  $\delta\mu$ . The perturbation of  $\delta\mu(n_B, \delta x, S)$  is thus

$$\Delta\delta\mu = \left. \frac{\partial\delta\mu}{\partial n_B} \right|_{\delta x, S} \Delta n_B + \left. \frac{\partial\delta\mu}{\partial \delta x} \right|_{n_B, S} \Delta\delta x. \quad (3)$$

At fixed density, a fluid element of *npe* matter that is out of beta equilibrium by a small amount  $\delta\mu$  adjusts its proton fraction back to its beta equilibrium value accordingly, to first order in  $\delta\mu$ ,

$$\frac{\partial\delta x}{\partial t} = \frac{\lambda_{n \leftrightarrow p}}{n_B} \delta\mu, \quad (4)$$

where

$$\lambda_{n \leftrightarrow p}(T, n_B) \equiv \left. \frac{\partial(\Gamma_{n \rightarrow p} - \Gamma_{p \rightarrow n})}{\partial\delta\mu} \right|_{\delta\mu=0}. \quad (5)$$

The decay rates (number of decays per volume per time)  $\Gamma_{n \rightarrow p}$  and  $\Gamma_{p \rightarrow n}$  are of the flavor-changing processes that inter-convert neutrons and protons, which in *npe* matter are the Urca processes, namely neutron decay and electron capture (D. G. Yakovlev et al. 2001). For small deviations from beta equilibrium, taking the time derivative of Equation (3) and then plugging in Equation (4), yields

$$\frac{\partial\Delta\delta\mu}{\partial t} = \left. \frac{\partial\delta\mu}{\partial n_B} \right|_{\delta x, S} \frac{\partial\Delta n_B}{\partial t} - \gamma \Delta\delta\mu, \quad (6)$$

where we have recast  $\lambda_{n \leftrightarrow p}$  as the beta equilibration relaxation rate  $\gamma$ , which is defined as

$$\gamma \equiv - \left. \frac{\lambda_{n \leftrightarrow p}}{n_B} \frac{\partial\delta\mu}{\partial \delta x} \right|_{n_B, S}, \quad (7)$$

which has a dimension of frequency and can be directly compared to the oscillation mode angular frequency  $\omega$ . The calculation of the susceptibility  $(\partial\delta\mu/\partial\delta x)|_{n_B, S}$  from the EOS tables, using  $n_B$ ,  $x$ , and  $T$  as input variables, is detailed in Appendix A.

The calculation of the rates in Equation (7) requires a microscopic model of nuclear matter that provides us not just with the EOS, but also with the dispersion relations of the nucleons. We calculate our results for three different EOSs, described below, in order to properly consider the range of possible *g*-mode physics.

In Figure 1, we plot the beta equilibration rate  $\gamma$  as a function of the baryon density. We include both the direct Urca processes ( $n \rightarrow p + e^- + \bar{\nu}_e$  and  $e^- + p \rightarrow n + \nu_e$ ) as well as the modified Urca processes ( $n + N \rightarrow p + e^- + \bar{\nu}_e + N$  and  $e^- + p + N \rightarrow n + \nu_e + N$ , where  $N$  is a neutron or proton). For simplicity, we calculate the rates of these processes in the Fermi surface approximation, which is valid for strongly degenerate nuclear matter (typically,  $T \lesssim 1$  MeV) (M. G. Alford & S. P. Harris 2018; M. G. Alford et al. 2021). In this limit, only particles on the Fermi surface participate in the reactions. This constraint on the phase space gives rise to a direct Urca threshold density: below this density, direct Urca is kinematically forbidden because the neutron Fermi momentum is too big relative to the proton and

electron Fermi momenta (equivalently, the proton fraction is too small). Modified Urca does not have such a density threshold and has a rate that is only weakly dependent on the baryon density (D. G. Yakovlev et al. 2001). As the temperature rises, the beta relaxation rate  $\gamma$  initially scales as  $T^4$  for the direct Urca process and as  $T^6$  for the modified Urca process. Above temperatures of a few MeV, thermal contributions from particles away from the Fermi surface begin to dominate the reaction rates, causing a blurring in the density of the direct Urca threshold (M. G. Alford & S. P. Harris 2018; M. G. Alford et al. 2021). The formulas for the Fermi surface approximation of the Urca rates are given in Appendices A and B of E. R. Most et al. (2024).

The rates shown in Figure 1 were calculated in matter described by three different EOSs, each built from a relativistic mean-field theory, QMC-RMF3 (M. G. Alford et al. 2022, 2023), IUFSU (F. J. Fattoyev et al. 2010), and IOPB-I (B. Kumar et al. 2018). All of them agree with current astrophysical and theoretical constraints on the EOS (R. Kumar et al. 2024), but differ in their predictions of the composition of *npe* matter, which leads to significantly different predictions of the Urca rates. Critically, they have different predictions for the direct Urca threshold. While QMC-RMF3 does not have a direct Urca threshold at all, IOPB-I has a threshold density of  $n_{B, \text{thr}} = 0.414 \text{ fm}^{-3}$ , and IUFSU a threshold density of  $n_{B, \text{thr}} = 0.655 \text{ fm}^{-3}$ .

At low density, in Figure 1, direct Urca is forbidden for all EOSs, and the rates are entirely due to modified Urca. As the density increases, the rates for two of the EOSs, IUFSU and IOPB-I, increase dramatically as the direct Urca threshold is passed. The QMC-RMF3 EOS always forbids direct Urca, as the proton fraction never rises above 1/9 (see J. M. Lattimer et al. 1991). Equilibration rates at two different temperatures ( $T = 1$  and 3 MeV) are shown: clearly, the equilibration rate is a strong function of temperature (see e.g., Figure 8 in S. P. Harris 2024). To the right of the main plot, we attached a plot of the oscillation frequencies of the *f*-mode and *g*-mode as a function of the *central density* of the NS (different from the *x*-axis of the left plot). This presentation allows us to compare the frequency of the density change in the matter  $\omega$  with the rate at which the beta equilibrium is restored  $\gamma$ . This ratio is the key quantity in determining the bulk-viscous damping of the oscillation modes and the disappearance of the *g*-mode at high temperature. Evidently, temperatures of a few MeV will make the beta equilibration rate comparable to the density oscillation frequency.

Applying the harmonic oscillation ansatz  $e^{i\omega t}$  for all perturbations in Equation (6), we obtain

$$\Delta\delta\mu = \frac{\left. \frac{\partial\delta\mu}{\partial n_B} \right|_{\delta x, S} \Delta n_B}{1 + \frac{\gamma}{i\omega}}. \quad (8)$$

We substitute Equation (8) into Equation (2), yielding

$$\Delta p = \frac{p\Gamma}{n_B} \Delta n_B, \quad (9)$$

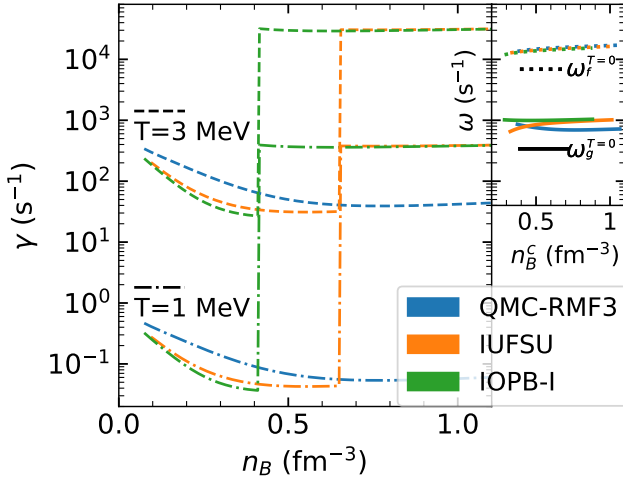


**Figure 1.** Left (main) panel shows the beta equilibration relaxation rate  $\gamma$  defined in Equation (7) for QMC-RMF3, IUFSU, and IOPB-I EOSs at temperatures  $T = 1$  MeV (dotted-dashed) and  $T = 3$  MeV (dashed). The solid (dashed) lines in the top right panel represent the  $g$ -mode ( $f$ -mode) frequency of cold NSs with various central baryon densities  $n_B^c$ . The sharp jump in the rate is due to the onset of the direct Urca threshold.

where the complex-valued effective adiabatic index for a damped oscillation of frequency  $\omega$  is given by

$$\Gamma = \frac{n_B}{p} \left[ \frac{\partial p}{\partial n_B} \bigg|_{\delta\mu, S} + \frac{\frac{\partial p}{\partial \delta\mu} \big|_{n_B, S} \frac{\partial \delta\mu}{\partial n_B} \big|_{\delta x, S}}{1 + \frac{\gamma}{i\omega}} \right]. \quad (10)$$

This expression can be recast in a more transparent form:

$$\Gamma = \Gamma_{\text{eq}} + \frac{\Gamma_{\text{ad}} - \Gamma_{\text{eq}}}{1 + \frac{\gamma}{i\omega}}, \quad (11)$$

$$\Gamma_{\text{ad}} = \frac{n_B}{p} \frac{\partial p}{\partial n_B} \bigg|_{\delta x, S}, \quad (12)$$

$$\Gamma_{\text{eq}} = \frac{n_B}{p} \frac{\partial p}{\partial n_B} \bigg|_{\delta\mu, S}, \quad (13)$$

where  $\Gamma_{\text{ad}}$  and  $\Gamma_{\text{eq}}$  characterize the compressibility of matter in the slow and fast limits of beta equilibration, respectively. The computation of these derivatives from the EOS tables, using  $n_B$ ,  $x$ , and  $T$  as input variables, is described in detail in Appendix A.

The dynamical sound speed squared  $c_{\text{dy}}^2$ , which incorporates finite-temperature viscous effects, is defined as

$$c_{\text{dy}}^2 = \frac{p}{\varepsilon + p} \Gamma = c_{\text{eq}}^2 + \frac{c_{\text{ad}}^2 - c_{\text{eq}}^2}{1 + \frac{\gamma}{i\omega}}, \quad (14)$$

where the equilibrium and adiabatic sound speed squared  $c_{\text{eq}}^2$  and  $c_{\text{ad}}^2$  are given by

$$c_{\text{eq}}^2 = \frac{p}{\varepsilon + p} \Gamma_{\text{eq}}, \quad c_{\text{ad}}^2 = \frac{p}{\varepsilon + p} \Gamma_{\text{ad}}. \quad (15)$$

The real and imaginary parts of the dynamical sound speed squared are then given by

$$\text{Re}[c_{\text{dy}}^2] = c_{\text{eq}}^2 + (c_{\text{ad}}^2 - c_{\text{eq}}^2) \frac{\omega^2}{\omega^2 + \gamma^2}, \quad (16)$$

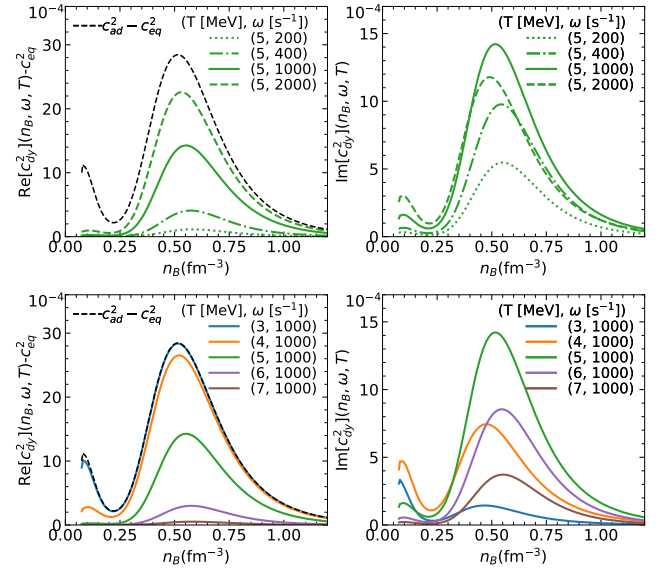


**Figure 2.** Real (left panels) and imaginary (right panels) part of the dynamical sound speed squared for the QMC-RMF3 EOS. For the real part, the equilibrium sound speed squared is used as a reference. The black dashed line represents the difference between adiabatic and equilibrium squared sound speeds. The upper two panels correspond to fixed temperature  $T = 5$  MeV while varying frequency  $\omega = [200, 400, 1000, 2000]$  s $^{-1}$ ; the bottom two panels represent fixed frequency  $\omega = 1000$  s $^{-1}$  while varying temperature from 3 to 7 MeV. Note the different scales of the y-axes in the real and imaginary parts.

$$\text{Im}[c_{\text{dy}}^2] = (c_{\text{ad}}^2 - c_{\text{eq}}^2) \frac{\omega\gamma}{\omega^2 + \gamma^2}. \quad (17)$$

The imaginary part,  $\text{Im}[c_{\text{dy}}^2]$ , is directly related to the bulk viscosity coefficient  $\zeta$ , which is defined via the energy dissipation rate  $d\varepsilon/dt = -\zeta(\nabla \cdot \mathbf{v})^2$ , since the bulk viscosity coefficient is also equal to the EOS-related factor times the resonance expression  $\gamma/(\gamma^2 + \omega^2)$  (S. P. Harris 2024). Using thermodynamic identities and the definitions of the adiabatic indices (Equations (12) and (13)), the bulk viscosity can be expressed as

$$\zeta = \frac{\varepsilon + p}{\omega} \text{Im}[c_{\text{dy}}^2] \quad (18)$$

$$= 4.5 \times 10^{29} \text{ g cm}^{-1} \text{ s}^{-1} \left( \frac{\omega}{600 \text{ s}^{-1}} \right)^{-1} \times \left( \frac{(\varepsilon + p)/c^2}{3 \times 10^{14} \text{ g cm}^{-3}} \right) \left( \frac{\text{Im}[c_{\text{dy}}^2]}{0.001} \right). \quad (19)$$

For NS matter, the adiabatic sound speed is usually very close to the equilibrium sound speed ( $c_{\text{ad}}^2 - c_{\text{eq}}^2 \lesssim 0.01$ ), and therefore the second term on the right-hand side of Equation (14) is small. As a result, the imaginary part of the dynamical sound speed squared is small, while the real part lies between the adiabatic and equilibrium squared sound speeds. The source of the difference between  $c_{\text{ad}}^2$  and  $c_{\text{eq}}^2$  in our paper is the gradient in the proton fraction  $x$ , not a gradient in the entropy per particle  $S$ , since we ignore finite-temperature effects in the EOS as justified in Appendix A. To demonstrate the dynamical sound speed squared  $c_{\text{dy}}^2$ , we plot the real and imaginary part of  $c_{\text{dy}}^2$  versus  $n_B$  for various temperatures  $T$  and frequencies  $\omega$  for the QMC-RMF3 EOS in Figure 2 and for the IOPB-I EOS in Figure 3. QMC-RMF3 shows double peaks in  $c_{\text{ad}}^2 - c_{\text{eq}}^2$  due to a plateau in the equilibrium composition  $x_{\text{eq}}$



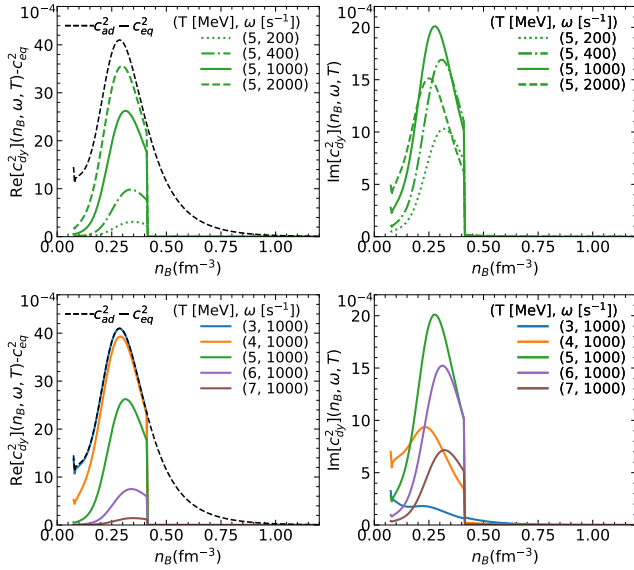


Figure 3. Same as Figure 2, but for the IOPB-I EOS.

around  $n_B = 0.2 \text{ fm}^{-3}$ . The IOPB-I curve only has one peak and terminates at  $n_B = 0.414 \text{ fm}^{-3}$ , beyond which  $c_{\text{dy}}^2 \approx c_{\text{eq}}^2$  due to the onset of the direct Urca process.

The real part of the dynamical sound speed is the adiabatic sound speed at low temperatures (or in the high-frequency limit), and as temperature is increased (or frequency is lowered), it decreases to the equilibrium sound speed. The imaginary part of the dynamical sound speed is nonmonotonic with respect to temperature—it starts from zero at low temperatures and then increases until reaching a peak at the resonant temperature where  $\gamma = \omega$ . As the temperature (and thus  $\gamma$ ) further increases, the imaginary part of the dynamical sound speed drops to zero. This resonant behavior is, naturally, just like the resonant behavior of bulk viscosity (S. P. Harris 2024).

In Figure 4, we show the maximum value (across all densities) of the imaginary part of the dynamical sound speed squared in the temperature-frequency plane. This plot depicts the resonant behavior described above. There is only one resonant peak for QMC-RMF3, while for IOPB-I, there exist two distinct resonant bands corresponding to the direct and modified Urca processes, respectively. These peaks are unrelated to the double-peak structure discussed in the context of Figure 2. The direct Urca process, with a higher reaction rate, has a resonant peak at a higher frequency or a lower temperature compared to the modified Urca process peak. Typical  $f$ -mode and  $g$ -mode frequencies at zero temperature are shown in Figure 4.

In this work, the crust EOSs in beta equilibrium are constructed with the compressible liquid droplet model with fixed surface tension parameters  $\sigma_s = 1.2 \text{ MeV fm}^{-2}$ ,  $S_s = 48 \text{ MeV}$  (J. M. Lattimer & F. D. Swesty 1991). Below the crust–core transition density, the adiabatic sound speed is set equal to the equilibrium sound speed, as our focus is on core  $g$ -modes following P. Jaikumar et al. (2021). This is justified because the adiabatic sound speed in the crust has only a limited impact on the properties of core  $g$ -modes (H. Sun et al. 2025).

### 3. Mode Equations

The components of the interior metric tensor for a spherically symmetric, nonrotating star are defined by

$$ds^2 = -e^{\nu(r)} dt^2 + e^{\lambda(r)} dr^2 + r^2(d\theta^2 + \sin^2\theta d\phi^2). \quad (20)$$

Following, e.g., P. Jaikumar et al. (2021), we solve the general relativistic nonradial mode equations in the relativistic Cowling approximation, which ignores perturbations of the metric tensor. The mode equations are

$$\frac{dU}{dr} = \frac{g}{c_{\text{dy}}^2} U + e^{\lambda/2} \left( \frac{l(l+1)}{\omega^2} e^\nu - \frac{r^2}{c_{\text{dy}}^2} \right) V, \quad (21)$$

$$\frac{dV}{dr} = e^{\lambda/2-\nu} \frac{\omega^2 - N^2}{r^2} U + g \left( \frac{1}{c_{\text{eq}}^2} - \frac{1}{c_{\text{dy}}^2} \right) V, \quad (22)$$

where  $U$  and  $V$  are related to the radial component of the Lagrangian displacement field  $\xi_r$  and the Eulerian perturbation of the pressure  $\delta p$  by

$$U = r^2 e^{\lambda/2} \xi_r, \quad V = \frac{\delta p}{\varepsilon + p}. \quad (23)$$

$l$  is the degree of the vector spherical harmonic representing the angular dependence of the displacement field, which we restrict to  $l=2$ . The gravitational acceleration  $g$  is

$$g = -\frac{1}{\varepsilon + p} \frac{dp}{dr} = \frac{1}{2} \frac{d\nu}{dr}. \quad (24)$$

The two sound speeds squared,  $c_{\text{eq}}^2$  and  $c_{\text{dy}}^2$ , are given by Equations (14) and (15). Note that  $c_{\text{dy}}^2$  replaces  $c_{\text{ad}}^2$  from the original formulation of the mode equations, which are recovered in the limit that  $\gamma \rightarrow 0$ . Finally, the Brunt–Väisälä frequency squared  $N^2$  is

$$N^2 = g^2 \left( \frac{1}{c_{\text{eq}}^2} - \frac{1}{c_{\text{dy}}^2} \right) e^{\nu-\lambda}. \quad (25)$$

Note that  $N^2$  is now complex and depends on  $\omega$  due to the inclusion of  $c_{\text{dy}}^2$ .  $N$  follows a similar temperature dependence as  $c_{\text{dy}}^2 - c_{\text{eq}}^2$  in Figures 2 and 3. Its real part decreases monotonically with increasing temperature, while the imaginary part starts from zero at zero temperature, increases to a maximum at  $\gamma = \sqrt{3} \omega$ , and then decreases with further temperature increase.

The boundary conditions at  $r=0$  are

$$U(r=0) = \frac{l}{\omega^2} Y_0 r^{l+1}, \quad (26)$$

$$V(r=0) = \frac{\varepsilon}{\varepsilon + p} Y_0 r^l, \quad (27)$$

where  $Y_0$  is a constant that shifts the overall amplitude of the oscillation mode, which is itself unconstrained. The  $r=R$  boundary condition is the vanishing of the Lagrangian pressure perturbation at  $\Delta p(r=R) = 0$ , which is equivalent to

$$0 = V(r=R) - \frac{1}{2R^2} U(r=R) e^{-\lambda(r=R)/2} \frac{d\nu}{dr} \Big|_{r=R}. \quad (28)$$

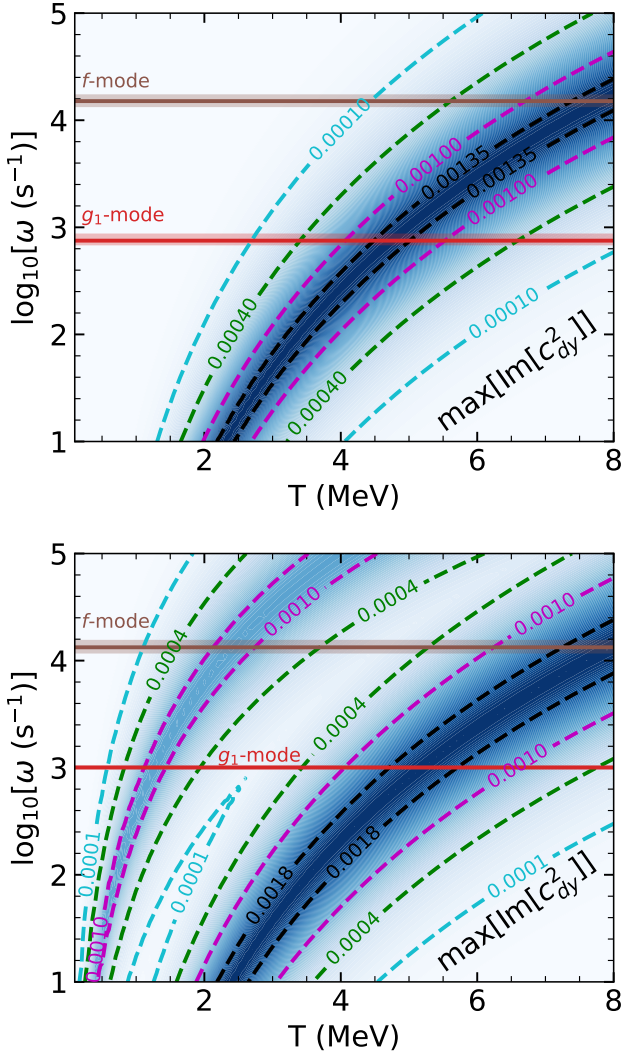


**Figure 4.** The dashed contour shows the maximum (across all densities) of the imaginary part of the dynamical sound speed squared for QMC-RMF3 (top) and IOPB-I (bottom). The dark blue region corresponds to the resonant peak, where bulk viscosity is most effective at damping oscillations. The horizontal brown and red bands represent typical  $f$ -mode and  $g_1$ -mode frequencies (at zero temperature) for NSs of various masses, with the central line corresponding to a  $1.4 M_\odot$  NS.

Since  $c_{dy}^2$  is complex, the solutions to the mode equations are also complex; therefore, Equations (21) and (22) can be solved by splitting them into real and imaginary parts. This is presented in Appendix B. We performed independent calculations of the oscillation modes using complex equations and then splitting into real and imaginary parts, obtaining identical results in each case.

To assess the validity of the relativistic Cowling approximation, we also carried out linearized full general relativity (GR) calculations of nonradial  $f$ -mode and  $g$ -modes, following the formalism outlined in the appendix of T. Zhao & J. M. Lattimer (2022). The system of differential equations governing linear nonradial oscillations in full GR reduces to Equations (21) and (22) of the relativistic Cowling approximation when the metric perturbations are neglected, as shown explicitly in T. Zhao et al. (2022). The main modification in this work is that we allow the adiabatic index or sound speed to

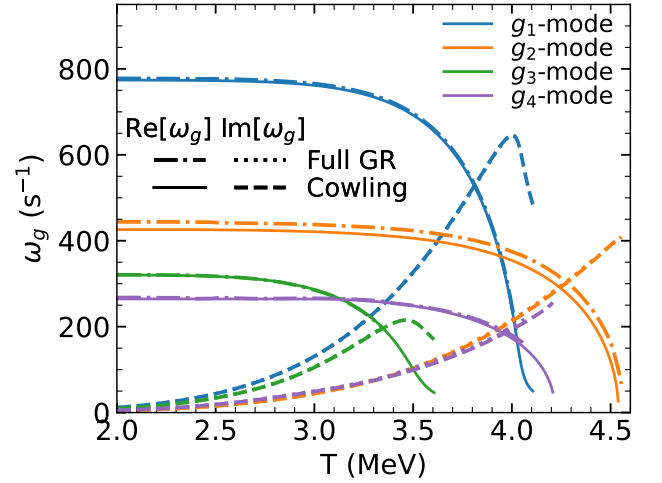


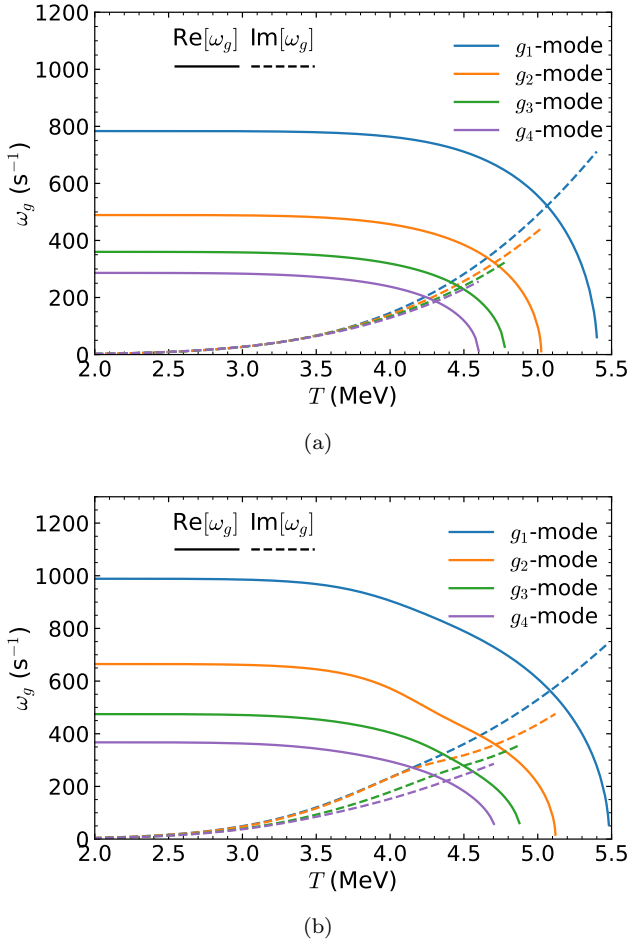
**Figure 5.** Real and imaginary parts of the frequencies of the fundamental and the first three overtone  $g$ -modes for a  $1.4 M_\odot$  NS vs. varying temperature for the QMC-RMF3 EOS. The imaginary part of the full GR calculation (dotted) largely overlaps with that of the calculation with Cowling approximation (dashed), and the real parts of the full GR calculation (dashed-dotted) and Cowling approximation (solid) are also very similar. We define the ordering of  $g$ -modes by their smooth asymptotic eigenmode at zero temperature.

be complex. We find the method of solving for eigenmodes based on root-finding of the amplitude of the ingoing gravitational wave component remains effective.

#### 4. Results

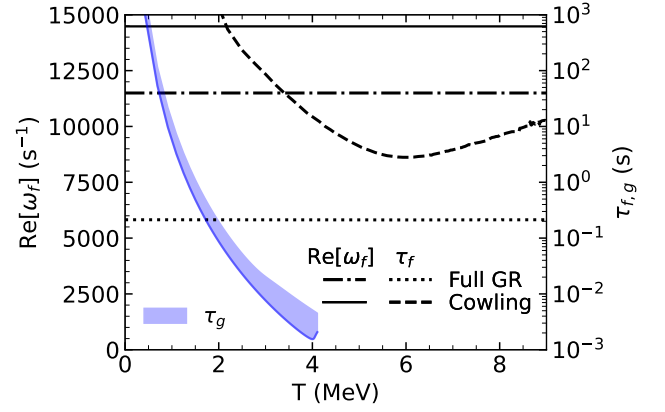
To examine the effect of weak interactions on the damping of  $g$ -modes, we computed the complex  $g$ -mode frequencies of  $1.4 M_\odot$  NSs at various temperatures for the three selected EOSs. First, a note on mode classification. A standard way to classify the oscillation modes of an NS is the Cowling scheme, based on (a) the restoring force for the mode ( $p$ ,  $f$ ,  $g$ , etc.), which determines the typical frequency range, and (b) the number of nodes of the mode's displacement field. We also follow this scheme to classify the  $g$ -modes, with a slight modification due to our inclusion of temperature-dependent bulk viscosity explicitly in the mode calculation. This modification is that we base our classification on the mode behavior at  $T = 0$ , and then continuously follow the same mode as the temperature is increased. For the complex frequency modes we study, the number of nodes can change as a function of temperature as the bulk viscous damping increases, the size of the imaginary part of the frequency increases and the real part decreases. However, we do not change the labeling of the mode as this happens: doing so results in a large number of changes in the mode labels at high temperature and is more confusing than clarifying. As long as we carefully follow each mode from zero temperature until the real part approaches zero, this classification is unambiguous. Since the mode frequencies are complex and well-separated in the complex plane, there are no avoided crossings between  $g$ -modes.

Figure 5 shows the real and imaginary parts of the  $g$ -mode frequency as a function of temperature for the QMC-RMF3 EOS, with the results compared between using and not using the Cowling approximation. The fundamental  $g$ -mode,  $g_1$ , which has one radial node, and the lowest three overtone  $g$ -modes  $\{g_2, g_3, g_4\}$ , with two, three, and four radial nodes,



**Figure 6.** Same as Figure 5 but for the IUFSU EOS (panel (a)) and the IOPB-I EOS (panel (b)).

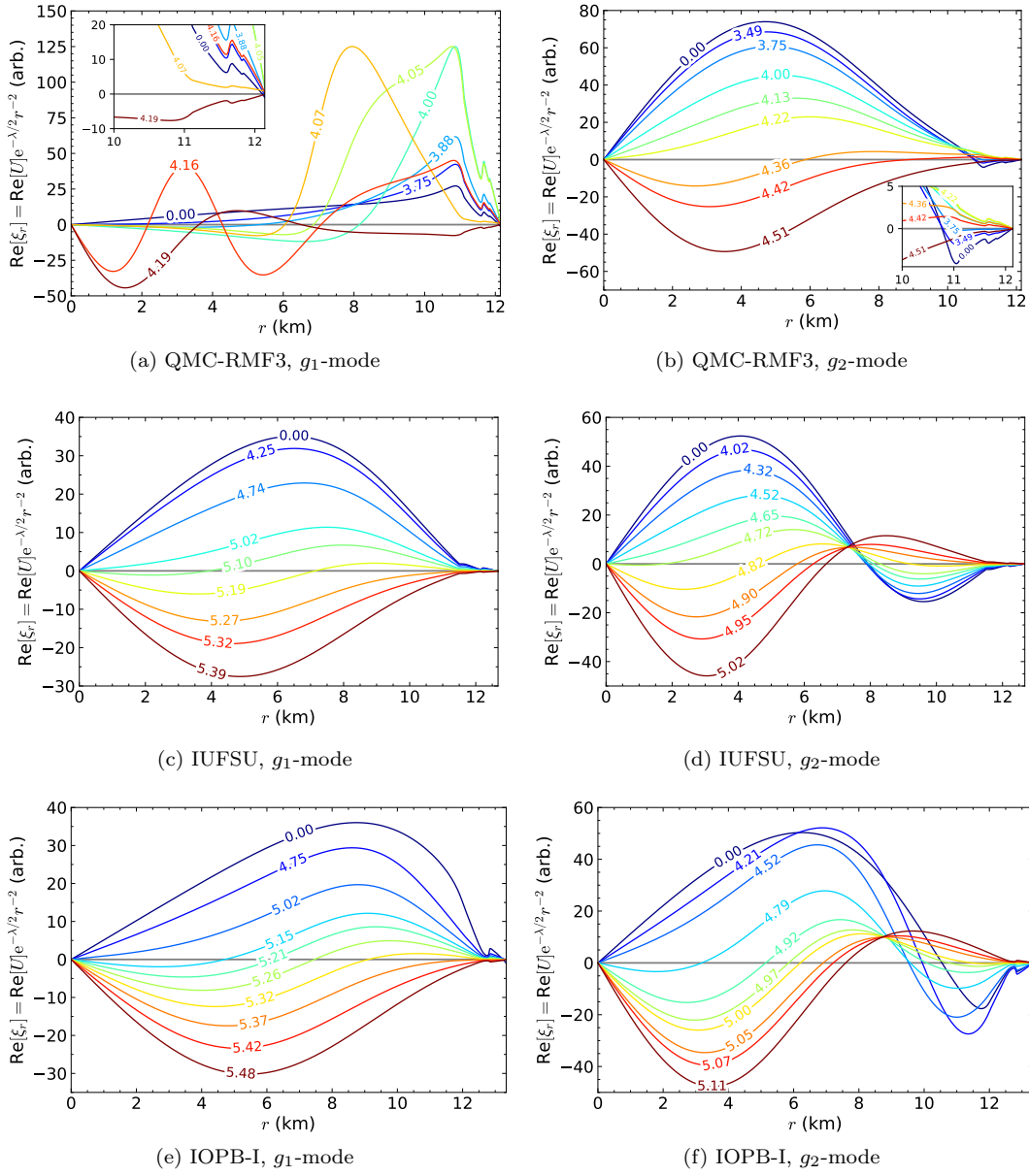
respectively, are shown. The Cowling approximation introduces only a very small error compared to the full GR calculation for the  $g$ -modes. Therefore, for the remainder of the paper we only consider results obtained using the Cowling approximation. As the temperature increases, the bulk viscosity rises until it reaches its resonant maximum around  $T \approx 5$  MeV, as can be read off from Figure 2. With rising temperature, the real part of the  $g$ -mode frequency decreases while the imaginary part increases. This is an interplay between the bulk viscosity, which dampens the modes, and the faster relaxation rates. In the limit of instantaneous relaxation, the restoring buoyant force vanishes, and thus the  $g$ -modes vanish. This behavior is expected, as the  $g$ -mode manifests as a global oscillation governed by the local Brunt–Väisälä frequency (Equation (25)). Since the beta relaxation rate  $\gamma$  increases rapidly with temperature, scaling as  $T^4$  for the direct Urca process and as  $T^6$  for the modified Urca process, the dynamical sound speed reduces to the equilibrium sound speed at high temperature according to Equations (16)–(17). Consequently, the Brunt–Väisälä frequency decreases with increasing temperature and ultimately vanishes. The real parts of the odd-overtone  $g$ -modes (those modes with an odd number of radial nodes) vanish at lower temperatures compared to the even  $g$ -modes because of the double peaks in the sound speed squared difference shown in Figure 2. This leads to an interchange in the temperature at which these modes vanish, such that the  $g_2$  and  $g_4$  modes vanish at higher



**Figure 7.** Frequency (solid and dotted-dashed) and damping time (dashed and dotted) of the  $f$ -mode calculated with and without Cowling approximation for the QMC-RMF3 EOS. The damping time of  $g$ -modes in Figure 5 is plotted as the blue region for comparison. The bottom of the blue region corresponds to the lowest-order  $g$ -mode.

temperatures than the  $g_1$  and  $g_3$  modes. In comparison, Figure 6 shows the  $g$ -mode frequencies for the IUFSU and IOPB-I EOSs. Since these two EOSs have only one peak in their squared sound speed differences, they do not display a characteristic difference between the odd and even  $g$ -modes like that shown for the QMC-RMF3 EOS.

We also calculated the  $f$ -mode of a  $1.4 M_\odot$  NS at various temperatures, as shown in Figure 7, and found that the  $f$ -mode frequency is extremely insensitive to temperature. The real part of the frequency calculated with the Cowling approximation is 26% larger than that with the full GR calculation, indicating that the Cowling approximation is less accurate for studying  $f$ -mode oscillations (H. Sotani & T. Takiwaki 2020; T. Zhao & J. M. Lattimer 2022; I. A. Rather et al. 2025). The imaginary part is much smaller, so the damping time  $\tau = 1/\text{Im}[\omega_f]$  is plotted instead. Since the Cowling approximation calculation ignores the damping due to gravitational waves completely, it results in a damping time  $\approx 10$  s, much larger than the gravitational-wave damping time of the  $f$ -mode,  $\approx 0.1$  s. Therefore, the damping introduced by bulk viscosity is much weaker than the damping from gravitational waves, even at the resonant peak shown in Figure 4. This is not surprising given that the  $f$ -mode represents the compressible extension of the classical Kelvin mode, which corresponds to the fundamental surface gravity oscillation of an incompressible sphere (W. T. L. Kelvin 1910). In the incompressible limit, the  $f$ -mode displacement becomes divergence-free with a radial dependence proportional to  $\xi_r \propto r^l$ , peaking near the stellar surface (S. Chandrasekhar 1960). Even in the compressible case, the  $f$ -mode maintains this qualitative structure with small divergence in Lagrangian fluid perturbation. As a result, the analytical solution for the Kelvin mode remains an excellent approximation to the  $f$ -mode frequency, even in full GR (T. Zhao & J. M. Lattimer 2022). Therefore, the fluid undergoes compression and expansion only in the Eulerian description but remains largely uncompressed in the Lagrangian viewpoint. The smallness of Lagrangian compression is consistent with our finding that bulk viscosity has little impact on the linear  $f$ -mode in dense nucleonic matter across a wide range of temperatures. In contrast, the inclusion of additional degrees of freedom, such as hyperons, can significantly increase the bulk viscosity compared to the  $npe$  estimate Equation (19) (D. D. Ofengeim et al. 2019; M. G. Alford &





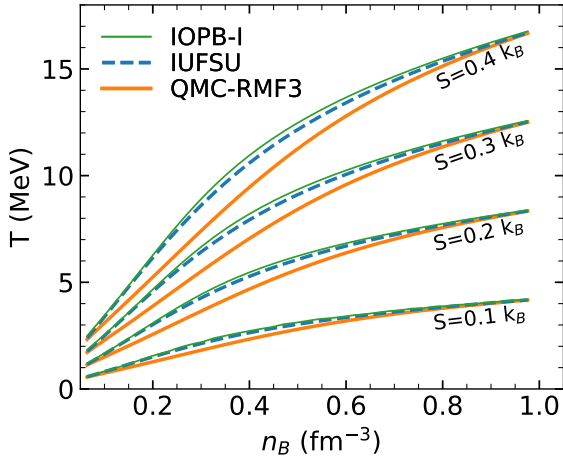


**Figure 9.** Temperature profiles at fixed entropy per baryon for three (QMC-RMF3, IUFSU, and IOPB-I) EOSs. These profiles are obtained by solving the equations of motion numerically in weak chemical equilibrium and at finite temperatures. At each density point, the entropy is calculated for several temperature points and then linearly interpolated in order to apply a root-finding algorithm to determine the desired constant entropy profile.

as shown in the zoomed-in insets, thus retaining a single internal node at first and then three nodes. At the highest temperatures examined, when the real part of the mode frequency becomes much smaller than the imaginary part, the displacement field has two nodes. The behavior of the first overtone mode displacement field in panel (b) also violates the typical behavior expected from Sturm–Liouville theory: as the temperature approaches  $T = 4$  MeV, the mode first becomes nodeless, with both its nodes near  $r \approx 11$  km and the outer boundary vanishing (this is difficult to distinguish even with the zoomed-in insets), then a new node develops at  $r = 0$ , moving to larger  $r$  as  $T$  increases. The mode has one and then two nodes again before both vanish at the highest temperature examined. The IUFSU and IOPB-I EOSs show similar behavior as seen in Figure 8 panels (c)–(f), with nodes appearing or disappearing as the temperature increases toward the limit where the imaginary part of  $\omega_g$  exceeds the real part. For completeness, we note that the imaginary parts of the displacement fields are shown in Appendix B. They exhibit a similar radial structure to the real parts, with amplitudes much smaller at low temperatures and becoming comparable only once the imaginary part of the mode frequency becomes significant at temperatures  $T \gtrsim 4$  MeV.

To investigate the impact of bulk viscosity on NSs with varying thermal structures (A. Kumar et al. 2024b; S. Ghosh et al. 2024b), we first compute temperature profiles at fixed entropy per baryon values,  $S = s/n_B = \{0.1, 0.2, 0.3, 0.4\} k_B$ , for three different EOSs as shown in Figure 9. In the degenerate limit of a neutron gas, the entropy per baryon follows the relation  $S = \pi^2 k_B^2 T m_L / k_F^2$ , where  $k_F = (3\pi^2 n_B)^{1/3}$  is the Fermi momentum, and the Landau effective mass is defined as  $m_L = k_F (dk_F / d\epsilon_F)$ , which reduces to  $m_L = \sqrt{k_F^2 + m_D^2}$ , where  $m_D$  is the Dirac effective mass in the RMF model. Consequently, at fixed entropy per baryon, the temperature scales as  $T \propto n_B^{2/3} / m_L$ , where the Landau effective mass  $m_L$  exhibits different density dependencies across the three EOSs. At subnuclear densities, where  $k_F \ll m_D$ , the Landau mass approaches  $m_L \approx m_D$ , yielding the scaling  $T \propto n_B^{2/3} / m_D$ . At several times nuclear saturation density, where  $k_F \gg m_D$ , one finds  $m_L \approx k_F \propto n_B^{1/3}$ , and the

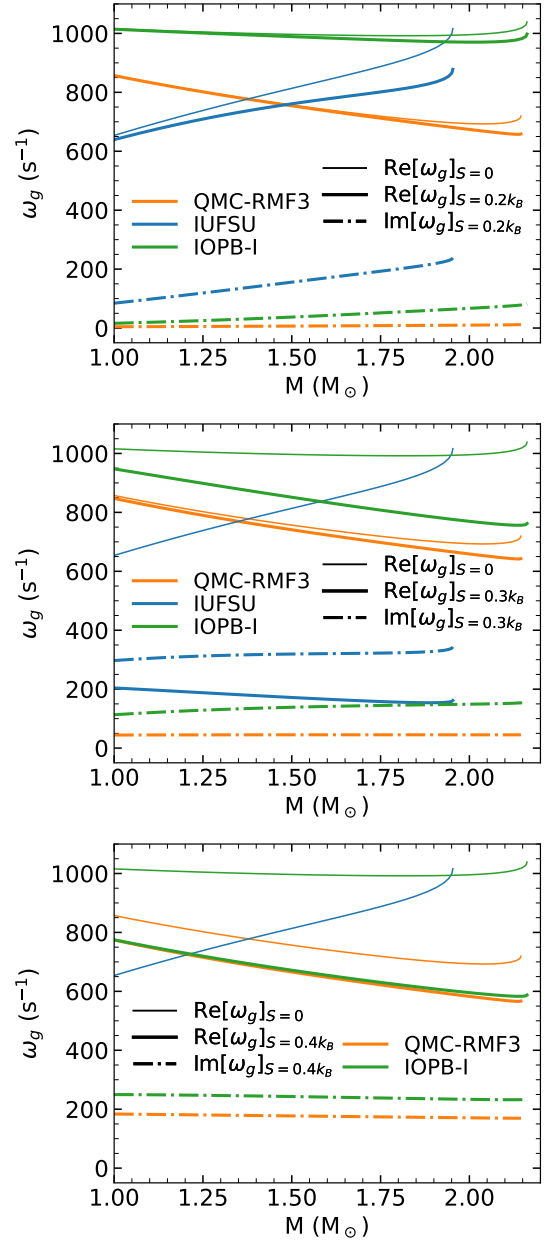


**Figure 10.**  $g_1$ -mode frequency as a function of NS mass at fixed entropy per baryon  $S = 0.2 k_B$  (top),  $S = 0.3 k_B$  (middle), and  $S = 0.4 k_B$  (bottom). The real (thick solid lines) and imaginary (dotted–dashed lines) parts of the frequency are shown, and the thin solid line refers to the cold adiabatic  $g$ -mode frequency in the absence of viscosity, which has no imaginary part. Results for three different EOSs are shown, and the calculations were performed within the Cowling approximation.

temperature scales as  $T \propto n_B^{1/3}$ . This trend of the power-law index decreasing from  $2/3$  to  $1/3$  appears in Figure 9.

Using these temperature profiles, we compute the  $g_1$ -mode frequencies as a function of the stellar mass, shown in Figure 10. For comparison, the zero entropy ( $T = 0$ )  $g_1$ -modes, which are purely real, are also shown as thin lines. The most notable feature is that the real part of the frequency for the  $g_1$ -mode with the IUFSU EOS decreases much more with increasing  $S$  than for the other two EOSs, such that it vanishes at  $S = 0.4 k_B$ . This can be explained by examining the temperature dependence of the sound speed squared difference  $c_{dy}^2 - c_{eq}^2$  for the IUFSU EOS and then comparing it to those obtained for the other two EOSs. At the crust–core transition

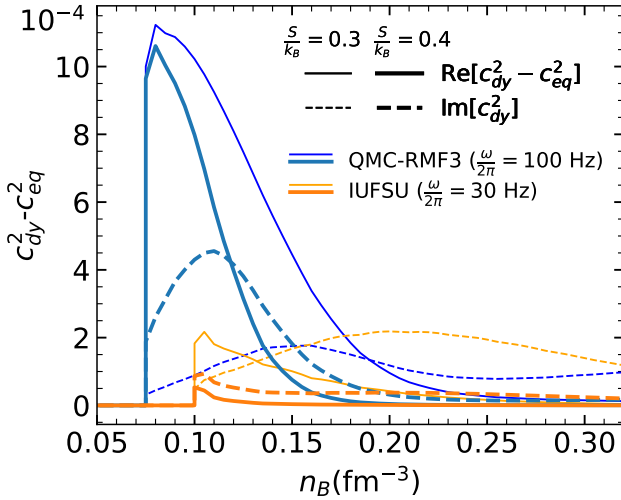


**Figure 11.** Real (solid) and imaginary (dashed) parts of the difference between the dynamical and equilibrium sound speed squared,  $\text{Re}[c_{\text{dy}}^2 - c_{\text{eq}}^2]$  and  $\text{Im}[c_{\text{dy}}^2]$ , as functions of the baryon number density  $n_B$  at fixed values of the entropy per baryon,  $S = 0.3 k_B$  (thin) and  $S = 0.4 k_B$  (thick). Results are shown for the QMC-RMF3 EOS at an oscillation frequency  $f = 100$  Hz (blue) and for the IUFSU EOS at  $f = 30$  Hz (orange). The density regions where  $\text{Re}[c_{\text{dy}}^2 - c_{\text{eq}}^2] > \text{Im}[c_{\text{dy}}^2]$  can support local  $g$ -mode oscillations, whereas regions dominated by the imaginary part indicate strong damping and therefore the mode propagation is suppressed.

density  $n_B \approx 0.08 \text{ fm}^{-3}$ , the constant entropy  $S = 0.4 k_B$  profile corresponds to a temperature  $T \approx 3 \text{ MeV}$  according to Figure 9. From Figures 2–3, for the QMC-RMF3 and IOPB-I EOSs, the real part of  $c_{\text{dy}}^2 - c_{\text{eq}}^2$  is larger than the imaginary part at this temperature and density. Though the density increases and the temperature for fixed  $S$  correspondingly increases deeper inside the star, the real part of  $c_{\text{dy}}^2 - c_{\text{eq}}^2$  being larger than the imaginary part near the crust–core transition is sufficient for the  $g_1$ -mode to be supported. However, for the IUFSU EOS, the real and imaginary parts of  $c_{\text{dy}}^2 - c_{\text{eq}}^2$  at  $T \approx 3 \text{ MeV}$  are already nearly the same, and since the imaginary part only becomes greater and the real part smaller as the density increases and the temperature simultaneously increases for fixed  $S$ , the  $g_1$ -mode vanishes for this and larger values of  $S$ . This is shown explicitly in Figure 11, which compares the real and imaginary parts of the sound speed squared difference for  $S = 0.3 k_B$  and  $0.4 k_B$  for the QMC-RMF3 and IUFSU EOSs as functions of the density, computed at values of  $\omega$  approximating the  $g_1$ -mode frequency. For both values of  $S$  for the QMC-RMF3 EOS, there is a region of the star where  $\text{Re}[c_{\text{dy}}^2 - c_{\text{eq}}^2] > \text{Im}[c_{\text{dy}}^2]$ , which is also the case for the IUFSU EOS when  $S = 0.3 k_B$ . However,  $\text{Im}[c_{\text{dy}}^2] > \text{Re}[c_{\text{dy}}^2 - c_{\text{eq}}^2]$  for the IUFSU EOS at  $S = 0.4 k_B$ , indicating that there is no  $g_1$ -mode for this EOS at this value of  $S$ .

## 5. Conclusions and Outlook

Thermal effects on the  $g$ -modes of NSs are of increasing interest because these modes will be excited in protoneutron stars and postmerger remnant NSs. In this work, we introduce the concept of the dynamical sound speed squared,  $c_{\text{dy}}^2$ , which captures the impact of bulk viscous effects in hot NS matter at temperatures of a few MeV. Unlike conventional adiabatic and equilibrium sound speeds, the dynamical sound speed incorporates the frequency-dependent damping effects of weak

interaction equilibration, leading to a complex-valued expression. The real part of  $c_{\text{dy}}^2$  lies between the equilibrium sound speed squared  $c_{\text{eq}}^2$  and the adiabatic sound speed squared  $c_{\text{ad}}^2$ , while its imaginary part encodes dissipative effects associated with the bulk viscosity,  $\zeta = \text{Im}[c_{\text{dy}}^2](\epsilon + P)/\omega$ . We demonstrate that the imaginary part  $\text{Im}[c_{\text{dy}}^2]$  exhibits a resonant peak when the beta equilibration rate  $\gamma$  becomes comparable to the oscillation frequency  $\omega$ . To further characterize this behavior, we identify the resonant region by mapping the peak values of  $\text{Im}[c_{\text{dy}}^2]$  (across varying densities) in the  $T$ – $\omega$  plane and then compare it to the characteristic frequencies of NS oscillation modes. For EOSs where direct Urca is kinematically forbidden on the Fermi surface (e.g., QMC-RMF3), we find a single resonance band that starts at zero frequency around  $T \approx 2 \text{ MeV}$  and extends to  $\omega = 100 \text{ Hz}$  at  $T \approx 4.5 \text{ MeV}$ , continuing beyond. In contrast, EOSs with a direct Urca threshold exhibit significantly faster beta equilibration rates  $\gamma$  at densities above the threshold, leading to an additional resonance band at lower temperatures or higher frequencies, as seen in the right panel of Figure 4 for IOPB-I.

In order to assess the relative importance of bulk viscous damping and GW damping, we employ both full GR calculations and the relativistic Cowling approximation, in which metric perturbations are neglected. We validate that the Cowling approximation remains a reliable and accurate method for computing  $g$ -modes, even when bulk viscosity is included, but it is less accurate for the  $f$ -mode.

Using these methods, we investigate the effects of weak interactions and bulk viscosity on the  $g$ -modes and  $f$ -mode of NSs by computing their complex frequencies at different temperatures. For  $g$ -modes, our results confirm that GW damping is negligible in comparison to bulk viscosity in warm NSs. As the temperature increases, bulk viscosity becomes more significant, leading to a decrease in the real part of the  $g$ -mode frequency as well as an increase in its imaginary part, indicating stronger damping. We observe that for EOSs with a double-peak structure in the sound speed squared difference (e.g., QMC-RMF3), the odd- and even-overtone  $g$ -modes behave differently, whereas EOSs with a single peak (e.g., IUFSU, IOPB-I) do not exhibit this distinction. Additionally, we find that at sufficiently high temperatures, bulk viscosity alters the nodal structure of the displacement field, deviating from the expectations of Sturm–Liouville theory, as modes develop additional nodes.

In contrast, we find that the  $f$ -mode frequency remains largely insensitive to temperature and that the bulk viscosity has a negligible effect on its damping compared to gravitational wave emission. This is consistent with the fact that the  $f$ -mode is the compressible extension of the incompressible Kelvin mode, which is nearly divergence-free. In the Lagrangian frame, fluid elements undergo minimal compression, significantly reducing the impact of bulk viscosity on the mode’s dissipation.

The relative insensitivity of the  $f$ -mode to bulk viscosity is crucial for understanding the gravitational-wave spectrum from postmerger remnants. Since the  $f$ -mode emits gravitational waves efficiently, the gravitational-wave peak frequency is often dominated by  $f$ -mode oscillations (H. H.-Y. Ng et al. 2021), and in such cases, the bulk viscosity is expected to have only a minor impact on the gravitational-wave signal, as suggested in D. Radice et al. (2022), F. Zappa et al. (2023). However, if the peak frequency contains nonlinear

contributions from other modes, e.g., radial modes (T. Soutanis et al. 2022), then the bulk viscosity may substantially alter both the postmerger dynamics and the emitted gravitational waves (E. R. Most et al. 2024; M. Chabanov & L. Rezzolla 2025).

Our analysis shows that at temperatures of a few MeV, beta equilibration becomes rapid enough to significantly affect the frequency and damping time of  $g$ -modes. In addition to examining  $g$ -modes at constant temperature, we also computed  $g$ -modes for NSs with constant entropy per baryon profiles. This approach provides a more realistic representation of the thermal structures in newly formed or merging NSs. We find that increasing the entropy per baryon generally leads to a decrease in the real part of the  $g$ -mode frequency, with the effect being most pronounced for the IUFSU EOS, where the frequency vanishes at  $S = 0.4 k_B$ , due to strong bulk viscous effects. This behavior is directly linked to the temperature dependence of the sound speed squared difference  $c_{dy}^2 - c_{eq}^2$ , which determines the strength of the restoring force for  $g$ -modes. For EOSs like QMC-RMF3 and IOPB-I, where the real part of  $c_{dy}^2 - c_{eq}^2$  remains larger than the imaginary part at relevant densities, the  $g$ -mode persists even at high entropy. However, for the IUFSU EOS, where the imaginary part dominates at all densities when the entropy per baryon reaches  $S = 0.4 k_B$ , the restoring force weakens, leading to the disappearance of the  $g_1$ -mode. These results highlight that both the  $g$ -mode frequency and its damping are highly sensitive to the thermal profile and the EOS when the temperature or entropy reaches the resonant peak of the bulk viscosity.

In our relativistic Cowling analysis, the  $f$ -,  $g$ -modes, and other uncalculated modes are treated as a linearly independent basis in the Hilbert space of fluid perturbations. Nonetheless, nonlinear coupling between these modes may become significant in the highly dynamic environment of NS mergers. In such scenarios, the bulk viscous damping of  $g$ -modes might indirectly influence the gravitational-wave signal via energy transfer or mode mixing with the dominant  $f$ -mode (H. Yu et al. 2023). Besides,  $g$ -modes play a critical role in the nonlinear saturation of unstable  $f$ -modes driven by the Chandrasekhar–Friedman–Schutz mechanism (S. Chandrasekhar 1970; J. L. Friedman & B. F. Schutz 1978). Specifically, coupling to stable  $g$ -modes provides a dissipation channel that limits the  $f$ -mode amplitude (P. Pnigouras & K. D. Kokkotas 2015). Our finding that bulk viscosity can strongly damp  $g$ -modes at  $T \gtrsim 5$  MeV suggests this saturation mechanism may be suppressed, potentially allowing the  $f$ -mode to grow to larger amplitudes than previously expected for cold NSs.

In the future, it is important to improve on the Fermi surface approximation of the Urca rates used in this work. Finite-temperature effects blur the direct Urca threshold, eliminating the sharp jump in the beta equilibration rate that occurs at the threshold density (M. G. Alford & S. P. Harris 2018; M. G. Alford et al. 2021). This would modify the dynamic speed of sound and thus the  $g$ -modes. In addition, a new method that consistently takes the in-medium collisions of the decaying nucleons into account, called the “nucleon width approximation” (M. G. Alford et al. 2024b), would further improve the calculation of the beta equilibration rate  $\gamma$ . On a different front, as the temperature rises above a few MeV, neutrino-trapping effects become important, and these should be taken into account.

Matter at high densities is likely to include other degrees of freedom, including muons (M. Alford et al. 2021; P. Jaikumar et al. 2021), pions (E. E. Kolomeitsev & D. N. Voskresensky 2015; B. Fore & S. Reddy 2020; V. Vijayan et al. 2023; S. P. Harris et al. 2025; M. A. Pajkos & E. R. Most 2025), hyperons (D. D. Ofengeim et al. 2019; M. G. Alford & A. Haber 2021; J. J. Li et al. 2023; V. Tran et al. 2023; A. Kumar et al. 2024a), deconfined quarks (A. Drago et al. 2005; M. G. Alford et al. 2019; C. Constantinou et al. 2023; H. Sotani & T. Kojo 2023; M. Alford et al. 2024; B. K. Pradhan et al. 2024), and perhaps dark matter (B. Fornal 2023; P. Routaray et al. 2023; S. Shirke et al. 2023; D. Sen & A. Guha 2024). These exotic particles have their own reaction channels that will contribute to chemical equilibration and will modify the bulk viscosity. Nevertheless, the dynamical sound speed introduced in this work provides a flexible framework that can incorporate such viscous effects in both radial and nonradial oscillation analyses (C. Zhang et al. 2024). Additionally, the existence of a first-order phase transition between hadronic and quark matter in hybrid stars gives rise to a discontinuity  $g$ -mode. Typically, this mode is calculated under the assumption that the quark–hadron conversion occurs arbitrarily slowly, similar to the historical development of compositional  $g$ -mode calculations (G. Miniutti et al. 2003; M. C. Rodríguez et al. 2021; T. Zhao & J. M. Lattimer 2022). However, quark–hadron conversion occurs at some finite, temperature-dependent rate, and we expect that accounting for this rate properly will alter the discontinuity  $g$ -mode frequency and damping time (see P. B. Rau & G. G. Salaben (2023) for a treatment of the analogous radial mode problem). Of course, the discontinuity  $g$ -mode would vanish in the limit of fast quark–hadron conversion (L. Tonetto & G. Lugones 2020).

Finally, to properly study the effects of weak interactions on  $g$ -modes in a physical context such as a core-collapse supernova or a binary NS merger, one must incorporate realistic, time-dependent thermal and density profiles from supernova and NS merger simulations (V. Ferrari et al. 2003; G. Camelió et al. 2017; H. Sotani & T. Takiwaki 2020). The thermal structure of a protoneutron star evolves dynamically, with significant changes in temperature, composition, and neutrino transport over short timescales. With these realistic profiles, one can study a new array of questions. For instance, in certain regions of a protoneutron star, where the local temperature and composition lead to thermal relaxation proceeding much faster than chemical equilibration, the conditions for the neutron finger instability may arise (S. W. Bruenn et al. 2004). Throughout this work, we assumed adiabatic compression, which excludes thermal relaxation and thereby keeps the oscillation stable against this instability. However, if the dynamical sound speed is defined at constant temperature rather than constant entropy, corresponding to the limit of very efficient thermal conduction, the onset of the neutron finger instability can be identified by examining the sign of the imaginary part of the dynamical sound speed. Thus, using numerical supernova profiles will allow for a more accurate assessment of how bulk viscosity affects oscillation modes in astrophysical scenarios.

### Acknowledgments

The authors thank Nils Andersson, Suprovo Ghosh, K. J. Kwon, and David Radice for their valuable feedback on the manuscript. We gratefully acknowledge the program



“Neutron Rich Matter on Heaven and Earth” (INT-22r-2a), and the joint INT-N3AS workshop “EOS Measurements with Next-Generation Gravitational-Wave Detectors” (INT-24-89W), both held at the Institute for Nuclear Theory, University of Washington for hospitality and stimulating discussions. This research was supported in part by the INT’s U.S. Department of Energy grant No. DE-FG02-00ER41132. T.Z. acknowledges support by the Network for Neutrinos, Nuclear Astrophysics and Symmetries (N3AS), through the National Science Foundation Physics Frontier Center, grant No. PHY-2020275. P.B.R. was supported by the Simons Foundation through a SCIECS postdoctoral fellowship (grant No. PG013106-02). A.H. acknowledges support by the U.S. Department of Energy, Office of Science, Office of Nuclear Physics, under Award No. DE-FG02-05ER41375. A.H. furthermore acknowledges financial support by the UKRI under the Horizon Europe Guarantee project EP/Z000939/1. The work of S.P.H. was supported by the National Science Foundation grant PHY 21-16686. C.C. acknowledges support from the European Union’s Horizon 2020 Research and Innovation Program under the Marie Skłodowska-Curie grant Agreement No. 754496 (H2020-MSCA-COFUND-2016 FELL-INT). The work of S.H. was supported by Startup Funds from the T.D. Lee Institute and Shanghai Jiao Tong University.

### Appendix A Thermodynamic Derivatives

In this section, we rewrite the thermodynamic derivatives in the main text to a basis of independent variables  $\{x, n_B, T\}$ , which are most convenient to calculate for a particular EOS. Recall, again, that  $S \equiv s/n_B$ ,  $x = n_p/n_B$ ,  $\delta x = x - x_{\text{eq}}$ . Since equilibrium composition is determined as  $x_{\text{eq}}(n_B, S)$ ,  $\partial \delta x$  is equivalent to  $\partial x$ . With the use of thermodynamic Jacobians, the derivatives in Equation (7) can be written as

$$\left. \frac{\partial \delta \mu}{\partial x} \right|_{n_B, S} = \left. \frac{\partial \delta \mu}{\partial x} \right|_{n_B, T} - \frac{\left. \frac{\partial \delta \mu}{\partial T} \right|_{x, n_B} \left. \frac{\partial S}{\partial x} \right|_{T, n_B}}{\left. \frac{\partial S}{\partial T} \right|_{x, n_B}}, \quad (\text{A1})$$

$$\left. \frac{\partial p}{\partial n_B} \right|_{x, S} = \left. \frac{\partial p}{\partial n_B} \right|_{x, T} - \frac{\left. \frac{\partial p}{\partial T} \right|_{n_B, x} \left. \frac{\partial S}{\partial n_B} \right|_{x, T}}{\left. \frac{\partial S}{\partial T} \right|_{x, n_B}}, \quad (\text{A2})$$

$$\left. \frac{\partial p}{\partial n_B} \right|_{\delta \mu, S} = \left. \frac{\partial p}{\partial n_B} \right|_{x, T} - \frac{A \left. \frac{\partial p}{\partial x} \right|_{n_B, T} - B \left. \frac{\partial p}{\partial T} \right|_{n_B, x}}{C}. \quad (\text{A3})$$

where

$$A = \left. \frac{\partial \delta \mu}{\partial n_B} \right|_{x, T} \left. \frac{\partial S}{\partial T} \right|_{n_B, x} - \left. \frac{\partial \delta \mu}{\partial T} \right|_{n_B, x} \left. \frac{\partial S}{\partial n_B} \right|_{x, T}, \quad (\text{A4})$$

$$B = \left. \frac{\partial \delta \mu}{\partial n_B} \right|_{x, T} \left. \frac{\partial S}{\partial x} \right|_{n_B, T} - \left. \frac{\partial \delta \mu}{\partial x} \right|_{n_B, T} \left. \frac{\partial S}{\partial n_B} \right|_{x, T}, \quad (\text{A5})$$

$$C = \left. \frac{\partial \delta \mu}{\partial x} \right|_{n_B, T} \left. \frac{\partial S}{\partial T} \right|_{x, n_B} - \left. \frac{\partial \delta \mu}{\partial T} \right|_{x, n_B} \left. \frac{\partial S}{\partial x} \right|_{n_B, T}. \quad (\text{A6})$$

The susceptibility (A1) and the compressibilities (Equations (A2) and (A3)) turn out to exhibit minimal temperature dependence in the NS core for temperatures  $T \lesssim 10$  MeV. Figure 12 illustrates the finite-temperature effects on these thermodynamic derivatives for the QMC-RMF3 EOS. The left panel shows the temperature-induced

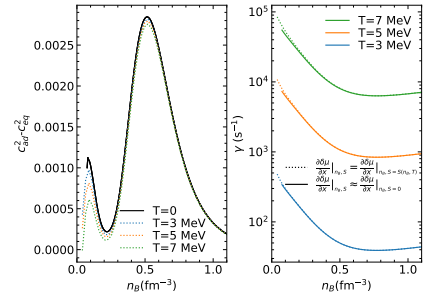


**Figure 12.** Left panel: the differences between the adiabatic and equilibrium sound speed squared  $c_{\text{ad}}^2 - c_{\text{eq}}^2$  around beta equilibrium  $x_{\text{eq}}(n_B, T)$ , as a function of the baryon density for various fixed-temperature profiles  $T = [0, 3, 5, 7]$  MeV for the QMC-RMF3 EOS. Right panel: the beta equilibration relaxation rate  $\gamma$  as a function of  $n_B$  for fixed-temperature profiles  $T = [3, 5, 7]$  MeV. The dotted lines follow the exact definition in Equation (7). The solid lines include finite-temperature effects in the beta reaction rate  $\lambda_{n \rightarrow p}$ , but approximate the susceptibility  $(\partial \delta \mu / \partial \delta x)|_{n_B, S}$  using its zero-temperature value.

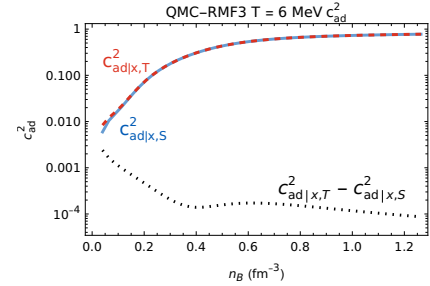


**Figure 13.** Isothermal (red, dashed) vs. constant specific entropy (blue) adiabatic speed of sound  $c_{\text{ad}}^2$  and their difference for the QMC-RMF3 EOS at a temperature of  $T = 6$  MeV. Even at temperatures in the upper range that we consider in this paper, the difference between the isothermal and the constant specific entropy  $c_{\text{ad}}^2$  is negligible, especially at larger densities.

variation in the sound speed squared difference,  $c_{\text{ad}}^2 - c_{\text{eq}}^2$ , which depends on the compressibilities. This variation is small compared to its zero-temperature reference value (black solid line), and is even smaller relative to the squared sound speeds themselves, particularly at high densities. Nevertheless, the difference at lower densities may have a more significant impact on crustal  $g$ -modes (F. Gittins & N. Andersson 2025). The right panel displays the beta equilibration relaxation rate  $\gamma$ , which depends on the susceptibility and the net decay rate as defined in Equation (5). The solid lines represent the full computation of  $\gamma$  from its definition in Equation (7), whereas the dashed lines correspond to calculations that neglect the temperature dependence of the susceptibility. The main finite-temperature contribution to  $\gamma$  arises from the net decay rates rather than the susceptibility. Therefore, in this work, we neglect the temperature dependence of the susceptibility and compressibilities and retain only the finite-temperature effects in the net decay rate. This approximation is employed in our calculations of both  $f$ -mode and  $g$ -modes.

Figure 13 shows a comparison of the adiabatic speed of sound from Equation (15) calculated at constant temperature  $T$  or constant specific entropy  $S$ . The relation between the required derivatives is shown in Equation (A2). While we are calculating the speed of sound at constant  $S$  in this work, the difference to the isothermal calculation is small, and only noticeable at densities below saturation densities, even at relatively high temperatures of  $T = 6$  MeV.



## Appendix B

### Real and Imaginary Parts Splitting of Mode Equations

To solve Equations (21) and (22) by splitting into real and imaginary parts, we take  $U = U_r + i U_i$ ,  $V = V_r + i V_i$  and  $\omega = \omega_r + i \omega_i$ . We also write Equation (11) as

$$\begin{aligned} \Gamma &= \Gamma_{\text{eq}} + \frac{\Gamma_{\text{ad}} - \Gamma_{\text{eq}}}{1 - \frac{\gamma}{\omega}} \\ &= \Gamma_{\text{eq}} + \frac{(\Gamma_{\text{ad}} - \Gamma_{\text{eq}})(\omega_r^2 + \omega_i(\omega_i - \gamma))}{\omega_r^2 + (\omega_i - \gamma)^2} \\ &\quad + i \frac{(\Gamma_{\text{ad}} - \Gamma_{\text{eq}})\omega_r\gamma}{\omega_r^2 + (\omega_i - \gamma)^2} \\ &\equiv \Gamma_r + i\Gamma_i, \end{aligned} \quad (\text{B1})$$

where  $\gamma$  is defined in Equation (7). Also defining the real and imaginary parts of  $N^2$  as

$$\begin{aligned} N^2 &= g^2 \frac{\varepsilon + p}{p} \left( \frac{1}{\Gamma_{\text{eq}}} - \frac{\Gamma_r}{\Gamma_r^2 + \Gamma_i^2} \right) e^{\nu-\lambda} \\ &\quad + i g^2 \frac{\varepsilon + p}{p} \left( \frac{\Gamma_i}{\Gamma_r^2 + \Gamma_i^2} \right) e^{\nu-\lambda} \equiv N_r + iN_i, \end{aligned} \quad (\text{B2})$$

the four mode equations we solve are

$$\begin{aligned} \frac{dU_r}{dr} &= \frac{(\varepsilon + p)g}{p(\Gamma_r^2 + \Gamma_i^2)} (\Gamma_r U_r + \Gamma_i U_i) \\ &\quad + e^{\lambda/2} \left( \frac{l(l+1)e^\nu(\omega_r^2 - \omega_i^2)}{(\omega_r^2 + \omega_i^2)^2} - \frac{(\varepsilon + p)r^2\Gamma_r}{p(\Gamma_r^2 + \Gamma_i^2)} \right) V_r \\ &\quad + e^{\lambda/2} \left( \frac{l(l+1)e^\nu 2\omega_r\omega_i}{(\omega_r^2 + \omega_i^2)^2} - \frac{(\varepsilon + p)r^2\Gamma_i}{p(\Gamma_r^2 + \Gamma_i^2)} \right) V_i, \end{aligned} \quad (\text{B3})$$

$$\begin{aligned} \frac{dU_i}{dr} &= \frac{(\varepsilon + p)g}{p(\Gamma_r^2 + \Gamma_i^2)} (-\Gamma_i U_r + \Gamma_r U_i) + e^{\lambda/2} \\ &\quad \times \left( -\frac{l(l+1)e^\nu 2\omega_r\omega_i}{(\omega_r^2 + \omega_i^2)^2} + \frac{(\varepsilon + p)r^2\Gamma_i}{p(\Gamma_r^2 + \Gamma_i^2)} \right) V_r \\ &\quad + e^{\lambda/2} \left( \frac{l(l+1)e^\nu(\omega_r^2 - \omega_i^2)}{(\omega_r^2 + \omega_i^2)^2} - \frac{(\varepsilon + p)r^2\Gamma_r}{p(\Gamma_r^2 + \Gamma_i^2)} \right) V_i, \end{aligned} \quad (\text{B4})$$

$$\begin{aligned} \frac{dV_r}{dr} &= \frac{e^{\lambda/2-\nu}}{r^2} [(\omega_r^2 - \omega_i^2 - N_r)U_r - (2\omega_r\omega_i - N_i)U_i] \\ &\quad + \frac{(\varepsilon + p)g}{p} \left[ \left( \frac{1}{\Gamma_{\text{eq}}} - \frac{\Gamma_r}{\Gamma_r^2 + \Gamma_i^2} \right) V_r - \frac{\Gamma_i}{\Gamma_r^2 + \Gamma_i^2} V_i \right], \end{aligned} \quad (\text{B5})$$

$$\begin{aligned} \frac{dV_i}{dr} &= \frac{e^{\lambda/2-\nu}}{r^2} [(2\omega_r\omega_i - N_i)U_r + (\omega_r^2 - \omega_i^2 - N_r)U_i] \\ &\quad + \frac{(\varepsilon + p)g}{p} \left[ \frac{\Gamma_i}{\Gamma_r^2 + \Gamma_i^2} V_r + \left( \frac{1}{\Gamma_{\text{eq}}} - \frac{\Gamma_r}{\Gamma_r^2 + \Gamma_i^2} \right) V_i \right]. \end{aligned} \quad (\text{B6})$$

The boundary conditions for the complex  $U$  and  $V$  cases are simply the real and imaginary parts of the real  $U$  and  $V$  boundary conditions. At  $r = 0$  we have

$$U_r(r = 0) = \frac{l(\omega_r^2 - \omega_i^2)}{(\omega_r^2 + \omega_i^2)^2} Y_0 r^{l+1}, \quad (\text{B7})$$

$$U_i(r = 0) = -\frac{2l\omega_r\omega_i}{(\omega_r^2 + \omega_i^2)^2} Y_0 r^{l+1}, \quad (\text{B8})$$

$$V_r(r = 0) = \frac{\varepsilon}{\varepsilon + p} Y_0 r^l, \quad (\text{B9})$$

$$V_i(r = 0) = 0, \quad (\text{B10})$$

and at  $r = R$  we have

$$0 = V_r(r = R) - \frac{1}{2R^2} U_r(r = R) e^{-\lambda(r=R)/2} \frac{d\nu}{dr} \Big|_{r=R}, \quad (\text{B11})$$

$$0 = V_i(r = R) - \frac{1}{2R^2} U_i(r = R) e^{-\lambda(r=R)/2} \frac{d\nu}{dr} \Big|_{r=R}. \quad (\text{B12})$$

Figure 8 in the main text shows the real part of the radial displacement field,  $U_r$ . For completeness, we display in Figure 14 the corresponding imaginary parts for the  $g_1$ -mode and  $g_2$ -mode, calculated for the QMC-RMF3, IUFSU, and IOPB-I EOSs. The imaginary parts exhibit radial structures similar to those of the real parts. At low temperatures their amplitudes are much smaller, but they grow and become comparable to the real parts once the imaginary part of the mode frequency is significant ( $T \gtrsim 4$  MeV).

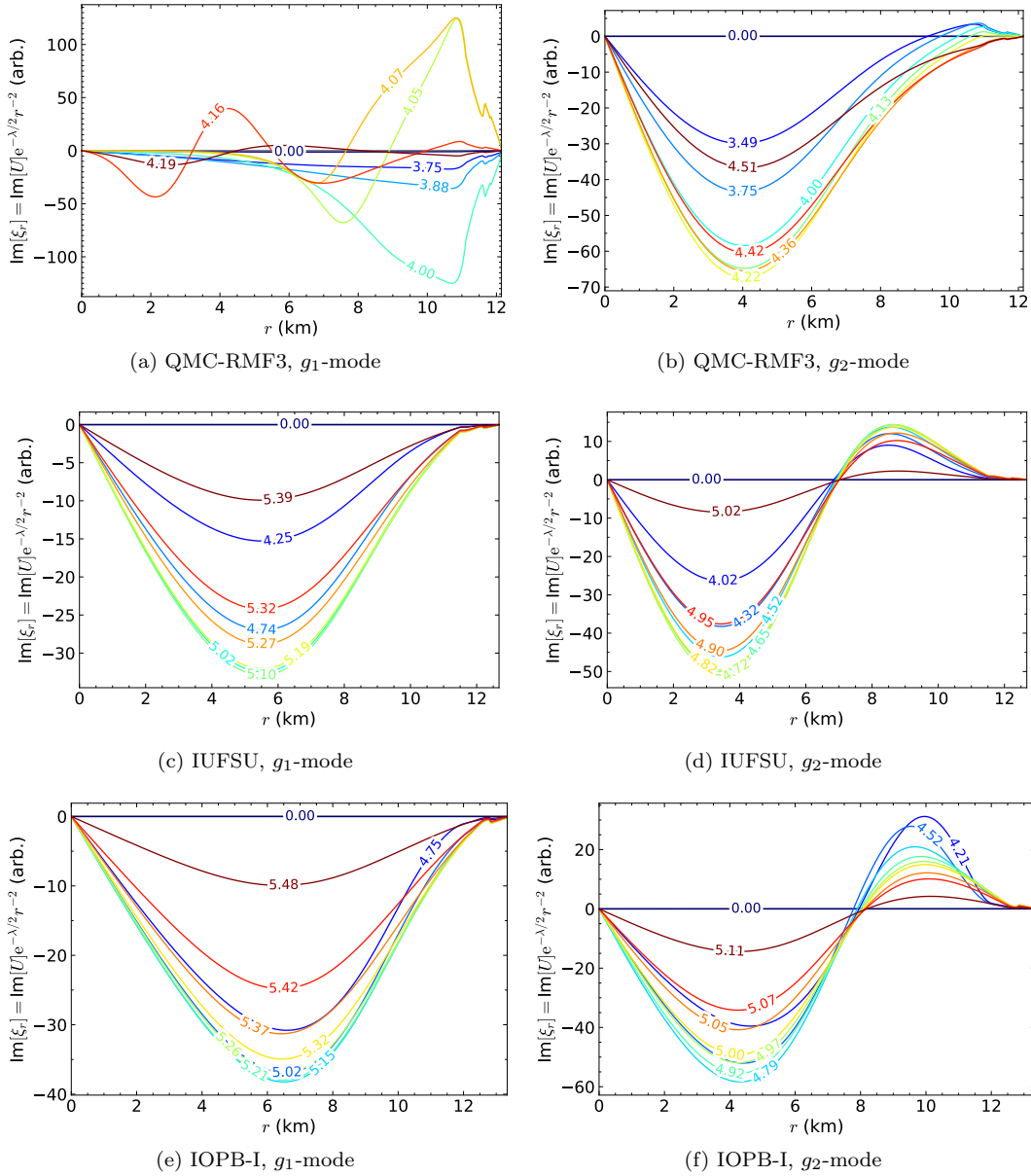


**Figure 14.** Imaginary part of the radial displacement field  $\xi_r(r)$  for the fundamental  $g_1$ -mode (left panels) and first overtone  $g_2$ -mode (right panels) as a function of the temperature, for three different EOSs: QMC-RMF3 (top row), IUFSU (middle row), and IOPB-I (bottom row).

### ORCID iDs

Tianqi Zhao <https://orcid.org/0000-0003-4704-0109>  
 Peter B. Rau <https://orcid.org/0000-0001-5220-9277>  
 Alexander Haber <https://orcid.org/0000-0002-5511-9565>  
 Steven P. Harris <https://orcid.org/0000-0002-0809-983X>  
 Constantinos Constantinou <https://orcid.org/0000-0002-4932-0879>  
 Sophia Han <https://orcid.org/0000-0002-9176-4617>

### References

- Alford, M., Harutyunyan, A., & Sedrakian, A. 2019, *PhRvD*, **100**, 103021  
 Alford, M., Harutyunyan, A., & Sedrakian, A. 2021, *PhRvD*, **104**, 103027  
 Alford, M., Harutyunyan, A., Sedrakian, A., & Tsiopelas, S. 2024, *PhRvD*, **110**, L061303  
 Alford, M. G., Brodie, L., Haber, A., & Tews, I. 2022, *PhRvC*, **106**, 055804  
 Alford, M. G., Bovard, L., Hanauske, M., Rezzolla, L., & Schwenzer, K. 2018, *PhRvL*, **120**, 041101  
 Alford, M. G., Brodie, L., Haber, A., & Tews, I. 2023, *PhysS*, **98**, 125302  
 Alford, M. G., & Haber, A. 2021, *PhRvC*, **103**, 045810  
 Alford, M. G., Haber, A., Harris, S. P., & Zhang, Z. 2021, *Univ*, **7**, 399  
 Alford, M. G., Haber, A., & Zhang, Z. 2024a, *PhRvC*, **109**, 055803  
 Alford, M. G., Haber, A., & Zhang, Z. 2024b, *PhRvC*, **110**, L052801  
 Alford, M. G., Han, S., & Schwenzer, K. 2019, *JPhG*, **46**, 114001  
 Alford, M. G., & Harris, S. P. 2018, *PhRvC*, **98**, 065806  
 Alford, M. G., & Harris, S. P. 2019, *PhRvC*, **100**, 035803  
 Andersson, N. 2019, *Gravitational-Wave Astronomy*, Oxford Graduate Texts (Oxford: Oxford Univ. Press)  
 Andersson, N., & Haskell, B. 2024, *Neutron Star Asteroseismology: Beyond the Mass-Radius Curve* (Boca Raton, FL: CRC Press)  
 Andersson, N., Kokkotas, K. D., & Schutz, B. F. 1999, *ApJ*, **510**, 846  
 Andersson, N., & Pnigouras, P. 2019, *MNRAS*, **489**, 4043  
 Arras, P., & Weinberg, N. N. 2019, *MNRAS*, **486**, 1424  
 Bruenn, S. W., Raley, E. A., & Mezzacappa, A. 2004, arXiv:astro-ph/0404099  
 Camelió, G., Gavassino, L., Antonelli, M., Bernuzzi, S., & Haskell, B. 2023a, *PhRvD*, **107**, 103031  
 Camelió, G., Gavassino, L., Antonelli, M., Bernuzzi, S., & Haskell, B. 2023b, *PhRvD*, **107**, 103032  
 Camelió, G., Lovato, A., Gualtieri, L., et al. 2017, *PhRvD*, **96**, 043015  
 Chabanov, M., & Rezzolla, L. 2025, *PhRvL*, **134**, 071402

- Chandrasekhar, S. 1969, *Ellipsoidal Figures of Equilibrium* (New Haven, CT: Yale Univ. Press)
- Chandrasekhar, S. 1970, *PhRvL*, **24**, 611
- Constantinou, C., Han, S., Jaikumar, P., & Prakash, M. 2021, *PhRvD*, **104**, 123032
- Constantinou, C., Zhao, T., Han, S., & Prakash, M. 2023, *PhRvD*, **107**, 074013
- Counsell, A. R., Gittins, F., & Andersson, N. 2024, *MNRAS*, **531**, 1721
- Counsell, R., Gittins, F., Andersson, N., & Pnigouras, P. 2024, *MNRAS*, **536**, 1967
- Dommes, V. A., & Gusakov, M. E. 2016, *MNRAS*, **455**, 2852
- Drago, A., Lavagno, A., & Pagliara, G. 2005, *PhRvD*, **71**, 103004
- Espino, P. L., Hammond, P., Radice, D., et al. 2024, *PhRvL*, **132**, 211001
- Fattoyev, F. J., Horowitz, C. J., Piekarewicz, J., & Shen, G. 2010, *PhRvC*, **82**, 055803
- Ferrari, V., Miniutti, G., & Pons, J. A. 2003, *MNRAS*, **342**, 629
- Fore, B., & Reddy, S. 2020, *PhRvC*, **101**, 035809
- Fornal, B. 2023, *Univ*, **9**, 449
- Friedman, J. L., & Schutz, B. F. 1978, *ApJ*, **222**, 281
- Ghosh, S., Pradhan, B. K., & Chatterjee, D. 2024a, *PhRvD*, **109**, 103036
- Ghosh, S., Shaikh, S., Kalita, P. J., et al. 2024b, *NuPhB*, **1008**, 116697
- Gittins, F., & Andersson, N. 2025, *PhRvD*, **111**, 083024
- Gourgoulhon, E., & Haensel, P. 1993, *A&A*, **271**, 187
- Gourgoulhon, E., Haensel, P., & Gondek, D. 1995, *A&A*, **294**, 747
- Gusakov, M. E., Yakovlev, D. G., & Gnedin, O. Y. 2005, *MNRAS*, **361**, 1415
- Harris, S. P. 2024, *Bulk Viscosity in Dense Nuclear Matter* (Boca Raton, FL: CRC Press)
- Harris, S. P., Fore, B., & Reddy, S. 2025, *PhRvC*, **111**, 015802
- Jaikumar, P., Sempowski, A., Prakash, M., & Constantinou, C. 2021, *PhRvD*, **103**, 123009
- Jakobus, P., Müller, B., Heger, A., et al. 2023, *PhRvL*, **131**, 191201
- Kantor, E. M., & Gusakov, M. E. 2014, *MNRAS*, **442**, 90
- Kelvin, W. T. L. 1910, *Mathematical and Physical Papers*, Vol. 4: *Hydrodynamics and General Dynamics* (Cambridge: Cambridge Univ. Press), 130
- Kolomeitsev, E. E., & Voskresensky, D. N. 2015, *PhRvC*, **91**, 025805
- Kumar, A., Ghosh, M. K., Thakur, P., et al. 2024a, *EPJC*, **84**, 692
- Kumar, A., Thakur, P., & Sinha, M. 2024b, *MNRAS*, **530**, 501
- Kumar, B., Agrawal, B. K., & Patra, S. K. 2018, *PhRvC*, **97**, 045806
- Kumar, D., Mishra, H., & Malik, T. 2023, *JCAP*, **02**, 015
- Kumar, R., Dexheimer, V., Jahan, J., et al. 2024, *LRR*, **27**, 3
- Kwon, K. J., Yu, H., & Venumadhav, T. 2024, arXiv:2410.03831
- Lai, D. 1994, *MNRAS*, **270**, 611
- Lattimer, J. M., Prakash, M., Pethick, C. J., & Haensel, P. 1991, *PhRvL*, **66**, 2701
- Lattimer, J. M., & Swesty, F. D. 1991, *NuPhA*, **535**, 331
- Li, J. J., Sedrakian, A., & Weber, F. 2023, *PhRvC*, **108**, 025810
- Lozano, N., Tran, V., & Jaikumar, P. 2022, *Galax*, **10**, 79
- McDermott, P. N., van Horn, H. M., & Scholl, J. F. 1983, *ApJ*, **268**, 837
- Miniutti, G., Pons, J. A., Berti, E., Gualtieri, L., & Ferrari, V. 2003, *MNRAS*, **338**, 389
- Morozova, V., Radice, D., Burrows, A., & Vartanyan, D. 2018, *ApJ*, **861**, 10
- Most, E. R., Haber, A., Harris, S. P., et al. 2024, *ApJL*, **967**, L14
- Ng, H. H.-Y., Cheong, P. C.-K., Lin, L.-M., & Li, T. G. F. 2021, *ApJ*, **915**, 108
- Ofengeim, D. D., Gusakov, M. E., Haensel, P., & Fortin, M. 2019, *PhRvD*, **100**, 103017
- Page, D., Lattimer, J. M., Prakash, M., & Steiner, A. W. 2004, *ApJS*, **155**, 623
- Pajkos, M. A., & Most, E. R. 2025, *PhRvD*, **111**, 043013
- Passamonti, A., Andersson, N., & Ho, W. C. G. 2016, *MNRAS*, **455**, 1489
- Pnigouras, P., & Kokkotas, K. D. 2015, *PhRvD*, **92**, 084018
- Pradhan, B. K., Chatterjee, D., & Alvarez-Castillo, D. E. 2024, *MNRAS*, **531**, 4640
- Radice, D., Bernuzzi, S., Perego, A., & Haas, R. 2022, *MNRAS*, **512**, 1499
- Raduta, A. R., Oertel, M., & Sedrakian, A. 2020, *MNRAS*, **499**, 914
- Rather, I. A., Marquez, K. D., Thakur, P., & Lourenço, O. 2025, *PhRvD*, **112**, 023013
- Rau, P. B., & Salaben, G. G. 2023, *PhRvD*, **108**, 103035
- Rau, P. B., & Wasserman, I. 2018, *MNRAS*, **481**, 4427
- Reisenegger, A., & Goldreich, P. 1992, *ApJ*, **395**, 240
- Roberts, L. F., & Reddy, S. 2017, *PhRvC*, **95**, 045807
- Rodríguez, M. C., Ranea-Sandoval, I. F., Mariani, M., Malfatti, G., & Guilera, O. M. 2021, *AN*, **342**, 305
- Routaray, P., Das, H. C., Sen, S., et al. 2023, *PhRvD*, **107**, 103039
- Sedrakian, A., & Clark, J. W. 2019, *EPJA*, **55**, 167
- Sen, D., & Guha, A. 2024, *PhRvD*, **110**, 103013
- Shirke, S., Ghosh, S., Chatterjee, D., Sagunski, L., & Schaffner-Bielich, J. 2023, *JCAP*, **12**, 008
- Sotani, H., & Kojo, T. 2023, *PhRvD*, **108**, 063004
- Sotani, H., & Takiwaki, T. 2020, *PhRvD*, **102**, 063025
- Soultanis, T., Bauswein, A., & Stergioulas, N. 2022, *PhRvD*, **105**, 043020
- Sun, H., Niu, J.-X., Li, H.-B., et al. 2025, *PhRvD*, **111**, 103019
- Tonetto, L., & Lugones, G. 2020, *PhRvD*, **101**, 123029
- Torres-Forné, A., Cerdá-Durán, P., Passamonti, A., & Font, J. A. 2018, *MNRAS*, **474**, 5272
- Tran, V., Ghosh, S., Lozano, N., Chatterjee, D., & Jaikumar, P. 2023, *PhRvC*, **108**, 015803
- Vartanyan, D., Burrows, A., Wang, T., Coleman, M. S. B., & White, C. J. 2023, *PhRvD*, **107**, 103015
- Vijayan, V., Rahman, N., Bauswein, A., Martínez-Pinedo, G., & Arbina, I. L. 2023, *PhRvD*, **108**, 023020
- Wei, W., Salinas, M., Klähn, T., Jaikumar, P., & Barry, M. 2020, *ApJ*, **904**, 187
- Wolfe, N. E., Fröhlich, C., Miller, J. M., Torres-Forné, A., & Cerdá-Durán, P. 2023, *ApJ*, **954**, 161
- Yakovlev, D. G., Kaminker, A. D., Gnedin, O. Y., & Haensel, P. 2001, *PhR*, **354**, 1
- Yu, H., & Weinberg, N. N. 2017, *MNRAS*, **464**, 2622
- Yu, H., Weinberg, N. N., Arras, P., Kwon, J., & Venumadhav, T. 2023, *MNRAS*, **519**, 4325
- Zappa, F., Bernuzzi, S., Radice, D., & Perego, A. 2023, *MNRAS*, **520**, 1481
- Zhang, C., Luo, Y., Li, H.-b., Shao, L., & Xu, R. 2024, *PhRvD*, **109**, 063020
- Zhao, T., Constantinou, C., Jaikumar, P., & Prakash, M. 2022, *PhRvD*, **105**, 103025
- Zhao, T., & Lattimer, J. M. 2022, *PhRvD*, **106**, 123002